Georgoulas, A, Andredaki, M and Marengo, M

An Enhanced VOF Method Coupled with Heat Transfer and Phase Change to Characterise Bubble Detachment in Saturated Pool Boiling

energies

MDPI

Article

An Enhanced VOF Method Coupled with Heat Transfer and Phase Change to Characterise Bubble Detachment in Saturated Pool Boiling

Anastasios Georgoulas *, Manolia Andredaki and Marco Marengo

Advanced Engineering Centre, School of Computing, Engineering and Mathematics, Cockcroft Building, Lewes Road, University of Brighton, Brighton BN2 4GJ, UK; M.Andredaki@brighton.ac.uk (M.A.); M.Marengo@brighton.ac.uk (M.M.)

* Correspondence: A.Georgoulas@brighton.ac.uk; Tel.: +44-01273-642-900

Academic Editor: Kamel Hooman

Received: 4 November 2016; Accepted: 20 February 2017; Published: 24 February 2017

Abstract: The present numerical investigation identifies quantitative effects of fundamental controlling parameters on the detachment characteristics of isolated bubbles in cases of pool boiling in the nucleate boiling regime. For this purpose, an improved Volume of Fluid (VOF) approach, developed previously in the general framework of OpenFOAM Computational Fluid Dynamics (CFD) Toolbox, is further coupled with heat transfer and phase change. The predictions of the model are quantitatively verified against an existing analytical solution and experimental data in the literature. Following the model validation, four different series of parametric numerical experiments are performed, exploring the effect of the initial thermal boundary layer (ITBL) thickness for the case of saturated pool boiling of R113 as well as the effects of the surface wettability, wall superheat and gravity level for the cases of R113, R22 and R134a refrigerants. It is confirmed that the ITBL is a very important parameter in the bubble growth and detachment process. Furthermore, for all of the examined working fluids the bubble detachment characteristics seem to be significantly affected by the triple-line contact angle (i.e., the wettability of the heated plate) for equilibrium contact angles higher than 45°. As expected, the simulations revealed that the heated wall superheat is very influential on the bubble growth and detachment process. Finally, besides the novelty of the numerical approach, a last finding is the fact that the effect of the gravity level variation in the bubble detachment time and the volume diminishes with the increase of the ambient pressure.

Keywords: two-phase flow; VOF method; OpenFOAM; pool boiling; phase change

1. Introduction

Boiling heat transfer is encountered in a wide field of applications, ranging from everyday life applications to more complex, industrial applications. Therefore, exact knowledge and understanding of the boiling process and its fundamental parameters and limitations are necessary for the design and optimisation of a wide range of thermal systems and technologies. Another quite important aspect regarding boiling heat transfer is the wide range of dimensional scales in the applications. Due to the difficulty of generalizing the various operative conditions, boiling heat transfer has been intensively studied in the past and is still the subject of ongoing research activities in many research groups all over the world.

In the past, many semi-empirical correlations have been developed based on a large number of experiments for different parameter ranges. However, the number of influencing parameters is very high and is further increased by new experiments deploying new experimental correlations. Therefore, in order to further improve the existing predictive tools, a deeper physical understanding of the boiling

processes for the various temporal and spatial scales is necessary [1]. Generally, a comprehensive physical understanding can be achieved by either highly resolved boiling experiments or by highly resolved numerical simulations. These two approaches should not be separated or competing. They should rather be used together, in order to allow a quantitative comparison and a better capacity in designing thermal systems.

During the last decades, the rapid advancement in the experimental technology led to the development of modern measuring instruments and techniques that significantly increased the spatial and temporal resolutions that can be resolved by laboratory experiments. This enabled the experimental investigation of local and instantaneous quantities such as the local wall temperature underneath a vapour bubble or the instantaneous heat transfer at the bubble foot during the boiling process. In particular, the use of thermo-chromic liquid crystals (TLCs) [2], indium-tin-oxide (ITO) transparent heaters in combination with high-speed imaging [3], high-speed infrared thermography and particle image velocimetry [4] as well as the use of micro-heater arrays to impose a constant temperature or constant heat flux boundary conditions [5] has offered more detailed insight regarding the transient character of boiling heat transfer. However, all these modern and high-resolution techniques are still not sufficient to completely understand the microscale heat transfer in the vicinity of the three-phase contact line (liquid–vapour–solid). In particular the temperature of the liquid surrounding the vapour bubble could not yet be measured with a satisfying resolution. The local wall temperature can be measured within a certain distance to the three-phase contact line, while the temperature in the liquid is measured only at certain points in the far-field. However, the use of micro-thermocouples and micro-piezoelectric pressure transducers (e.g., [6,7]) is a quite promising approach to overcome such problems.

With the growing computing capabilities and the amount of available computing resources, as well as with the rapid development of modern numerical methods for the simulation of multi-phase flows, the numerical simulation of boiling heat transfer has become possible for a wide range of applications as well as spatial and temporal scales. In the recent years, the use of CFD codes has been extended to the analysis of three-dimensional, multi-phase flows, aiming to overcome the weakness of 1D numerical models. Typically, up until now, there are two main branches in the literature for the numerical investigation of boiling heat transfer by the use of CFD.

In the first branch, most of the existing open-source, in-house, and especially commercial CFD codes have adopted a Eulerian multi-phase flow approach, based on a two-fluid model. With this approach, there is a need to incorporate phase interaction terms such as sources/sinks in the governing equations which are usually calculated from problem-specific empirical closure relationships. Moreover, for the case of boiling flows, these global multi-phase CFD models are usually also coupled with appropriate wall boiling sub-models, such as the most widely used wall partitioning model of Kurul and Podowski [8]. Conversely, such wall boiling sub-models require additional closure relationships to predict, for example, the bubble departure characteristics and the density of the active nucleation sizes, incorporating a number of model constants, the value of which can be found only for specific flow conditions and working fluids. Recently, in the work of Prabhudharwadkar et al. [9] and Cheung et al. [10], the performance of a wide combination range of the existing closure relationships was examined through comparison with a wide range of experimental data. It is stated that no single combination of empirical correlations provides satisfactory predictions covering the entire range of the simulated conditions.

In the second branch, a complete or "direct" numerical simulation of the complex spatial and temporal evolution of the interface between the two phases is followed, utilising a variety of interface tracking/capturing approaches.

Unverdi and Tryggvason [11] and Tryggvason et al. [12] applied the front tracking (FT) method for the simulation of boiling heat transfer. The method showed very accurate predictions, especially in the calculation of the liquid-vapour interface curvature, which is vital for the simulation of boiling flows. However, the FT method was mainly used for the simulation of film boiling [13,14].

The Arbitrary Lagrangian-Eulerian (ALE) method was applied by Fuchs et al. [15], in order to simulate the transient characteristics in the pool boiling of binary mixtures. The heat flow at a growing bubble was calculated by utilising a boundary-fitted mesh. One important aspect of boundary-fitted meshes is the possibility to treat the liquid-vapour interface as a boundary of the computational domain, facilitating the estimation of the heat flux at the interface and therefore of the evaporation rate.

The Volume of Fluid (VOF) method can be considered as the most popular interface-capturing approach and it has also been used so far for the simulation of boiling flows. Welch and Rachidi [16] extended the VOF-based model of Welch and Wilson [17], adding transient heat conduction in the solid wall and simulated film boiling. Aus der Wiesche [18] used the VOF method to simulate the nucleate pool boiling of water. Hardt and Wondra [19] proposed a method for implementing phase change in a VOF or Level Set (LS) approach and performed simulations of film boiling and droplet evaporation using a VOF method. Ose and Kunugi [20,21] conducted sub-cooled pool boiling simulations and validated the numerical results by their own visualisation experimental data. Kunkelmann et al. [22] implemented a specific sub-model for micro-layer evaporation in their previously developed, user-defined diabatic VOF solver of the open-source CFD package OpenFOAM [23]. Detailed information on the proposed numerical method can be also found in Kunkelmann's PhD thesis [24]. A VOF-based sharp-interface phase change model was also presented in the work of Sato and Niceno [25]. In the proposed work, the Conservative Semi-Lagrangian Constrained Interpolation Profile method (CIP-CSL) was used to solve the advection equation of the colour function.

Son et al. [26] investigated the heat transfer associated with a single bubble during nucleate pool boiling by application of the LS method. In the same decade, many studies were also conducted by Dhir and co-workers for a variety of boiling flows, summarised by Dhir [27]. A considerable number of more recent works on boiling heat transfer have also been published which utilise the LS method for boiling heat transfer numerical investigations (e.g., [28]). A LS-based sharp interface capturing method for incompressible multi-phase flows with phase change is presented in the work of Gibou et al. [29]. In the proposed work, the LS method was utilised for interface tracking between the two phases in conjunction with a ghost fluid approach for imposing the jump conditions at the interface. A similar approach, but further enhanced in order to account both for boiling flows and liquid evaporation, was recently presented in the work of Villegas et al. [30]. Finally, in a recent work by Tanguy et al. [31], the efficiencies of the Ghost Fluid and Delta Function methods in a LS-based framework were compared through benchmark cases for the case of boiling flows.

The advantages of the VOF and LS methods have, in many cases, been combined in order to be applied for the simulation of boiling heat transfer–related problems, leading to CLSVOF (Combined Level Set and Volume of Fluid). For example, Shu [32], in his PhD thesis, applied the CLSVOF method to simulate boiling heat transfer using the open-source CFD package OpenFOAM, performing 2D simulations. The CLSVOF method was also used in the work of Kunkelmann and Stefan [33]. Apart from the coupling of their previously developed VOF approach with the LS method, in the proposed work the authors also modified the calculation of the local evaporation source term deviating from the originally proposed calculation of Hardt and Wondra [19]. Other quite different approaches such as the Lattice Boltzmann method [34] and the Phase Field method [35] have been also applied for the simulation of boiling heat transfer.

In the present investigation, an enhanced VOF-based numerical model that utilises a smoothing technique in order to suppress the development of spurious velocities in the vicinity of the interface, which was previously presented, validated and applied to the investigation of adiabatic bubble dynamics in the work of Georgoulas et al. [36], is further extended for the simulation of diabatic, liquid-vapour flows with phase change. In more detail, an energy transport equation and the phase change model, originally proposed by Hardt and Wondra [19], are further implemented to the proposed solver. The adopted phase change model [19] has been also utilised in previous similar investigations (e.g., [23,24,37]). The model is initially verified against an analytical solution and is also validated

against experimental results of pool boiling of refrigerants available in the literature [38]. Then, the validated and optimised version of the model is further applied for the conduction of a wide range of parametric numerical experiments, identifying the effects of the initial thermal boundary layer (ITBL) thickness, the surface wettability (triple-line contact angle), the plate superheat and the gravity level on the bubble detachment characteristics.

2. Numerical Method

2.1. Governing Equations

In this section, the governing equations for the mass, momentum, energy, and volume fraction are presented. It should be mentioned that the liquid and vapour phases are both treated as incompressible, Newtonian fluids. Apart from the liquid phase, which is obviously incompressible, for all of the cases presented in the present paper, the maximum flow velocity within the vapour phase did not exceed some meters per second. Therefore, the Mach number is safely low in order to neglect the compressibility effects and treat both phases as incompressible.

The mass conservation equation is given as:

$$\nabla \cdot \left(\rho \vec{U} \right) = \dot{\rho}, \tag{1}$$

where U is the fluid velocity and ρ is the bulk density. The source term on the right-hand side accounts for the phase change. It should be mentioned that despite the local source terms, the mass is globally conserved since all of the mass that is removed from the liquid side of the interface is added on the vapour side.

The conservation of momentum is given by the following equation:

$$\frac{\partial}{\partial t}\left(\rho \vec{U} \right) + \nabla \cdot \left(\rho \vec{U} \vec{U} \right) - \nabla \cdot \left\{ \mu \left[\nabla \vec{U} + \left(\nabla \vec{U} \right)^T \right] \right\} = -\nabla p + \vec{f}_{ST} + \vec{f}_g, \tag{2}$$

where p is the pressure and μ is the bulk dynamic viscosity. The momentum source terms on the right-hand side of the equation account for the effects of surface tension and gravity, respectively. The surface tension term is modelled according to the classical approach of Brackbill et al. [39].

The conservation of energy balance is given by the following equation:

$$\frac{\partial}{\partial t}\left(\rho c_p T \right) + \nabla \cdot \left(\vec{U} \rho c_p T \right) - \nabla \cdot \left(\lambda \nabla T \right) = \dot{h}, \tag{3}$$

where c_p is the bulk heat capacity, T is the temperature field, and λ is the bulk thermal conductivity. The source term on the right-hand side of the equation will be explained in Section 2.2.

The volume fraction α is advected by the flow field using the following equation:

$$\frac{\partial \alpha}{\partial t} + \nabla \cdot \left(\alpha \vec{U} \right) - \nabla \cdot \left(\alpha (1-\alpha) U_r \right) = \frac{\dot{\rho}}{\rho} \alpha, \tag{4}$$

Interface sharpening is very important in simulating two-phase flows of two immiscible fluids. In OpenFOAM, the sharpening of the interface is achieved artificially by introducing the extra compression term in Equation (4) ($\nabla \cdot (\alpha(1-\alpha)U_r)$), where U_r is the artificial compression velocity which is calculated from the following relationship:

$$U_r = n_f \min \left[C_\gamma \frac{|\varphi|}{|S_f|}, \max \left(\frac{|\varphi|}{|S_f|} \right) \right], \tag{5}$$

where n_f is the cell surface normal vector, φ is the mass flux, S_f is the surface area of the cell, and C_γ is a coefficient the value of which can be set between 1 and 4. Then U_r is the relative velocity between the two fluid phases due to the density and viscosity change across the interface. In Equation (4), the divergence of the compression velocity U_r ensures the conservation of the volume fraction α, while the term $\alpha(1-\alpha)$ limits this artificial compression approach only in the vicinity of the interface, where $0 < \alpha < 1$ [40]. The level of compression depends on the value of C_γ ([40,41]). For the simulations of the present investigation, initial trial simulations indicated that a value of $C_\gamma = 1$ should be used in order to maintain a quite sharp interface without at the same time having unphysical results. The source term on the right-hand side of the Equation (4) is needed because, due to the local mass source terms, the velocity field is not free of divergence.

It should be mentioned that the VOF method in OpenFOAM does not solve Equation (4) implicitly, but instead by applying a multidimensional universal limiter with an explicit solution algorithm (MULES). Together with the interface compression algorithm, this method ensures a sharp interface and bounds the volume fraction values between 0 and 1 [42].

Finally, the bulk fluid properties γ are computed as the averages over the liquid (γ_l) and vapour (γ_v) phases, weighted with the volume fraction α:

$$\gamma = \alpha\gamma_l + (1-\alpha)\gamma_v, \tag{6}$$

As it is known, the VOF method usually suffers from non-physical spurious currents in the interface region. These spurious velocities are due to errors in the calculation of the normal vectors and the curvature of the interface that are used for the calculation of the interfacial forces. These errors emerge from the fact that in the VOF method, the interface is implicitly represented by the volume fraction values that encounter sharp changes over a thin region [43].

As previously mentioned in the Introduction section of the present paper, the VOF-based solver that is used in the present investigation has been modified accordingly in order to account for an adequate level of spurious current suppression. The proposed modification involves the calculation of the interface curvature κ using smoothed volume fraction values $\widetilde{\alpha}$ which are obtained from the initially calculated volume fraction field α, smoothing it over a finite region in the vicinity of the interface:

$$\kappa = \nabla \cdot \left(\frac{\nabla \widetilde{\alpha}}{|\nabla \widetilde{a}|} \right), \tag{7}$$

All other equations are using the initially calculated (non-smoothed) volume fraction values of α. The proposed smoothing is achieved by the application of a Laplacian filter which can be described by the following equation:

$$\widetilde{\alpha}_p = \frac{\sum \alpha_f S_f}{\sum S_f}, \tag{8}$$

In Equation (8), the subscripts p and f denote the cell and face index, respectively, and α_f is the linearly interpolated value of α at the face center. The application of the proposed filter can be repeated more than one time in order to obtain an adequately smoothed field. For the applications of the present investigation, initial trial simulations indicated that the filter should be applied no more than two times, in order to avoid the levelling out of high curvature regions. The proposed, enhanced VOF solver has been tested and verified against experimental results of isothermal bubble dynamics available in the literature with an excellent degree of convergence. More details on the proposed validation as well as on the proposed improved VOF method can be found in the paper by Georgoulas et al. [36].

2.2. Phase Change Model

The utilised phase change model which was implemented in the improved OpenFOAM VOF solver that is used in the present investigation will be described briefly in this section. Supplementary details can be found in the work of Hardt and Wondra [19].

The evaporating mass flux at the liquid-vapour interface j_{evap} is calculated from the following equation:

$$j_{evap} = \frac{T_{int} - T_{sat}}{R_{int} h_{lv}}, \tag{9}$$

where T_{int} is the temperature of the interface, T_{sat} is the saturation temperature, R_{int} is the interfacial heat resistance and h_{lv} is the latent heat of evaporation at the saturation temperature.

The interfacial heat resistance is calculated by the following equation based in the considerations of Schrage [44],

$$R_{int} = \frac{2 - \gamma}{\gamma} \frac{\sqrt{2\pi R_{gas}}}{h_{lv}^2} \frac{T_{sat}^{3/2}}{\rho_v}, \tag{10}$$

It is clear that this last equation is in fact a fitting function, due to the uncertainty of the parameter γ, which eventually may vary in the range $0 < \gamma < 1$. For the cases that will be presented here, the constant γ which is also known as the evaporation/condensation coefficient is taken equal to unity from the literature (e.g., [22–24,33,45,46]). However, it should be noted that in different cases that are not presented in the present investigation, the value of the proposed coefficient needed to be significantly lower than unity. R_{gas} is the specific gas constant of the working fluid that is calculated from the universal gas constant and the molecular weight of the working fluid. The amount of liquid that evaporates is calculated locally and the resulting source term field is smeared over a few cells in order to avoid numerical instabilities. The evaporating mass is taken away on the liquid side of the interface and reappears on the vapour side. According to previous investigations (e.g., [22–24,33,45,46]), despite the fact that Equations (9) and (10) are derived from considerations on length scales which are several orders smaller than the typical grid size used in the simulations, the proposed evaporation model leads to correct evaporation rates since it acts as a control loop. The more the temperature at the interface deviates from the saturation value, the more liquid evaporates and the more the temperature drops locally. This ensures that the temperature at the liquid-vapour interface always remains close to the saturation temperature.

The evaporating/condensing mass flux is calculated from Equation (9) and must be incorporated into the conservation equations, by the definition of volumetric source terms. This is done by multiplying the evaporating mass flux at the liquid-vapour interface by the magnitude of the volume fraction gradient, as indicated in the following equation:

$$\dot{\rho}_0 = j_{evap} |\nabla a|, \tag{11}$$

This initial sharp source term field (SSTF) is integrated over the whole computational domain to calculate the "Net Mass Flow" through the entire liquid-vapour interface, using the following equation:

$$\dot{m}_{int} = \iiint \dot{\rho}_0 \mathrm{d}V, \tag{12}$$

This value is important for global mass conservation, in order to ensure that the magnitudes of the mass sources in the liquid and vapour parts are equal and correspond to the net evaporation rate. The sharp source term field is then smeared over several cells, by solving the following diffusion equation for the smooth distribution of source terms

$$\dot{\rho}_1 - \nabla \cdot \left[(D\Delta\tau) \nabla \dot{\rho}_1 \right] = \dot{\rho}_0, \tag{13}$$

where $\Delta\tau$ is an artificial time step and Neumann boundary conditions are imposed for the smooth source term field on all boundaries of the domain. Therefore, the integral values of the sharp and the smooth source fields remain the same, despite the smearing. The width of the smeared source term field is proportional to the square root of the product of the diffusion constant "D" and the artificial time step "$\Delta\tau$". It should be mentioned that the value of "D" must be adjusted to the mesh resolution such that the source term field is smeared over several cells.

Then, the source terms in all cells that do not contain pure liquid or vapour ($\alpha < 1 - \alpha_{cut}$ and $\alpha > \alpha_{cut}$, where α_{cut} may be set to 0.05) are artificially set to zero. This cropping step ensures that source terms are shifted into the pure vapour and liquid cells are only in the vicinity of the interface. The interface therefore is not subjected to any source terms and is only transported by the calculated velocity field. Therefore, the transport algorithm for the volume fraction field as well as the associated interface compression can work efficiently without any interference with the source term field. The remaining source term field is scaled individually on the liquid and the vapour side through the application of appropriate scaling coefficients. This scaling step ensures that the mass is globally conserved and that the evaporating or condensing mass flow corresponds globally to the net mass flow through the interface.

The newly proposed scaling coefficients N_l and N_v are calculated by integrating the smooth source term field in each of the pure phases and comparing it to the net mass flow $\dot{m}_{int}$ (Equation (12)), utilising the following equations:

$$N_l = \dot{m}_{int} \left[\iiint (\alpha - 1 + a_{cut}) \dot{\rho}_1 \mathrm{d}V \right]^{-1}, \tag{14}$$

$$N_v = \dot{m}_{int} \left[\iiint (a_{cut} - \alpha) \dot{\rho}_1 \mathrm{d}V \right]^{-1}, \tag{15}$$

Finally, the final source term distribution is calculated using the above scaling factors in the following equation:

$$\dot{\rho} = N_v(\alpha_{cut} - a)\dot{\rho}_1 - N_l(a - 1 + \alpha_{cut})\dot{\rho}_1, \tag{16}$$

An example of the aforementioned final source term distribution is depicted indicatively in Figure 1 below.

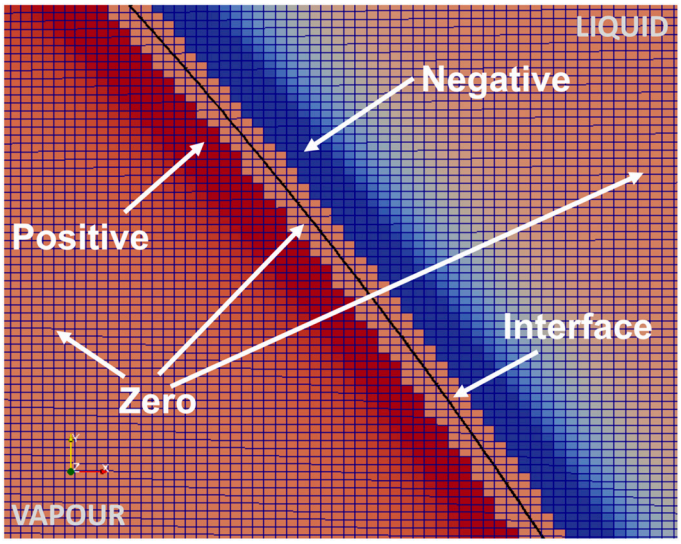

Figure 1. Distribution of the final source terms in the computational domain for the case of an evaporating bubble.

The source term $\dot{h}$ of Equation (3) is obtained from Equation (17):

$$\dot{h} = \left[N_v(1 - \alpha)C_{pv} - N_l \alpha C_{pl} \right] \dot{\rho}_1 T - \dot{\rho} h_{lv}, \tag{17}$$

where C_{pv} and C_{pl} represent the heat capacity of the vapour and liquid phases, respectively. The first part of the source term corresponds to a correction source term that removes artefacts that emerge due to the structure or the mass source term in the proposed methodology. The second part of the source

term represents the contribution of the enthalpy of evaporation or else the cooling associated with the latent heat of the phase change. Further details can be found in the work of Hardt and Wondra [19].

2.3. Simulation Parameters

As mentioned previously, all the numerical simulations on pool boiling of the present work were performed with the finite volume–based CFD code OpenFOAM (version 2.2.1), utilising and enhancing its original VOF-based solver "interFoam". For pressure-velocity coupling, the PISO (Pressure-Implicit with Splitting of Operators) scheme is applied. The transient terms in the equations are discretised using a second-order, bounded, implicit scheme (Euler). The calculation time step is controlled by setting the maximum Courant number to 0.2. With this adaptive time-stepping technique, the time step is automatically varied from approximately 10^{-9} to 10^{-6} s for the overall simulation cases that are presented in the present paper. The gradient terms are discretised using a second-order, Gaussian integration with linear interpolation (Gauss linear). For the divergence terms, different discretisation schemes are applied for each term in the equations. In more detail, the convection term of Equation (2) is discretised using a "Gauss upwind" scheme. The $\nabla \cdot \left(\alpha \vec{U} \right)$ term of Equation (4) is discretised using the "Gauss vanLeer" scheme, while the $\nabla \cdot (\alpha(1-\alpha)U_r)$ term is discretised using the "Gauss interfaceCompression" scheme which ensures the boundedness of the calculated volume fraction field. Finally, all Laplacian terms are discretised using the "Gauss Linear Corrected" scheme. The divergence term of Equation (3) is discretised using a "Gauss linear" scheme. Further details regarding the adopted discretisation schemes can be found in OpenFOAM Documentation (OpenFOAM, 2013 [42]). It should be mentioned that this was the optimum combination of discretisation schemes in order to maintain a balance between accuracy, convergence and numerical stability during the computations.

3. Validation of Numerical Method

3.1. Growth of a Spherical Bubble in a Superheated Liquid

The first test case that was selected in order to validate the previously described implementations in the improved VOF-based numerical model is the growth of a spherical bubble in an infinitely extended superheated liquid domain. This test case constitutes a widely used test case for the validation of boiling models throughout the literature (e.g., [19,23,37,46–48]).

The growth of the bubble within a superheated liquid domain follows two distinct stages. At the initial stage, the bubble growth is mainly controlled by the effects of surface tension and inertia. At the second stage, the growth is controlled only by the heat transfer rate from the superheated liquid to the liquid-vapour interface. During this final stage, it can be assumed that the bulk vapour and the liquid-vapour interface are at saturation temperature. The bubble size at this stage is quite large in order to safely neglect the vapour saturation temperature rise due to the pressure jump across the interface [46]. More details regarding the simulated phenomenon are described in detail in the work of Plesset and Zwick [47]. An analytical solution for this situation has been derived by Scriven [48]. According to this analytical solution, the bubble radius as a function of time is given by the following equation:

$$R(t) = 2\beta\sqrt{Dt} \tag{18}$$

where β is a growth constant, the details of which can be found in the work of Scriven [48], and D is the thermal diffusivity of the liquid. This analytical solution permits the calculation of the initial conditions for the numerical simulations (initial temperature profile at the bubble interface and initial bubble radius) in order to validate the numerical results. Here, all the details for the initial conditions of the simulations that are going to be presented are taken from the works of Kunkelmann and Stefan [23] and Magnini [46], which were derived from the above-mentioned analytical solution [48] for the time instant that the bubble in each case has a radius of 0.1 mm. The geometric characteristics and the initial conditions of the considered physical problem are illustrated schematically in Figure 2.

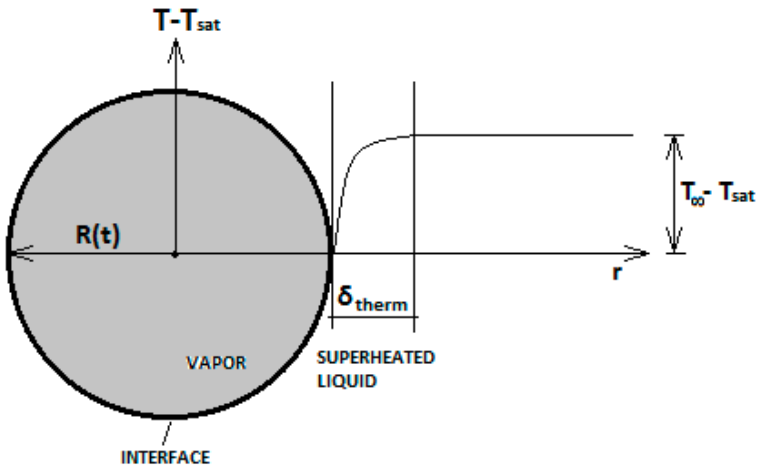

Figure 2. Schematic illustration of the geometrical characteristics and the initial conditions of the simulated validation cases.

Two-dimensional axisymmetric simulations were performed for three different working fluids, water and FC-72 liquid at equilibrium with their corresponding vapour phases (saturation point), at a pressure value of 1013 mbar, as well as R134a liquid at equilibrium with its vapour phase at a pressure value of 840 mbar. Uniform hexahedral grids of a 1 μm cell dimension were used in all three cases. The computational domain and grid that was constructed as well as the applied boundary conditions are depicted in Figure 3. The initial conditions for the water liquid/vapour case are illustrated in Figure 4, while the material properties and the initial conditions for all fluid cases are summarised in Table 1.

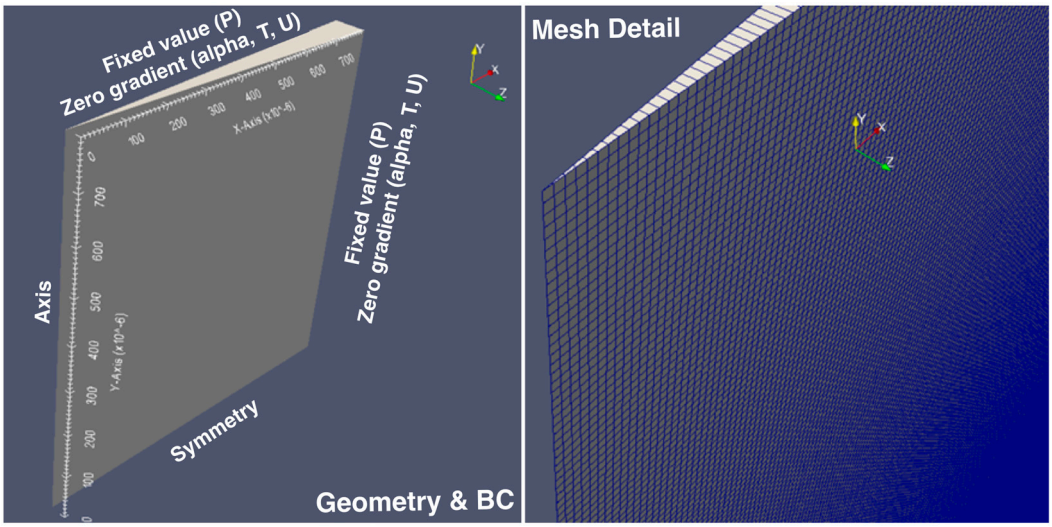

Figure 3. Two-dimensional axisymmetric computational domain, mesh and boundary conditions.

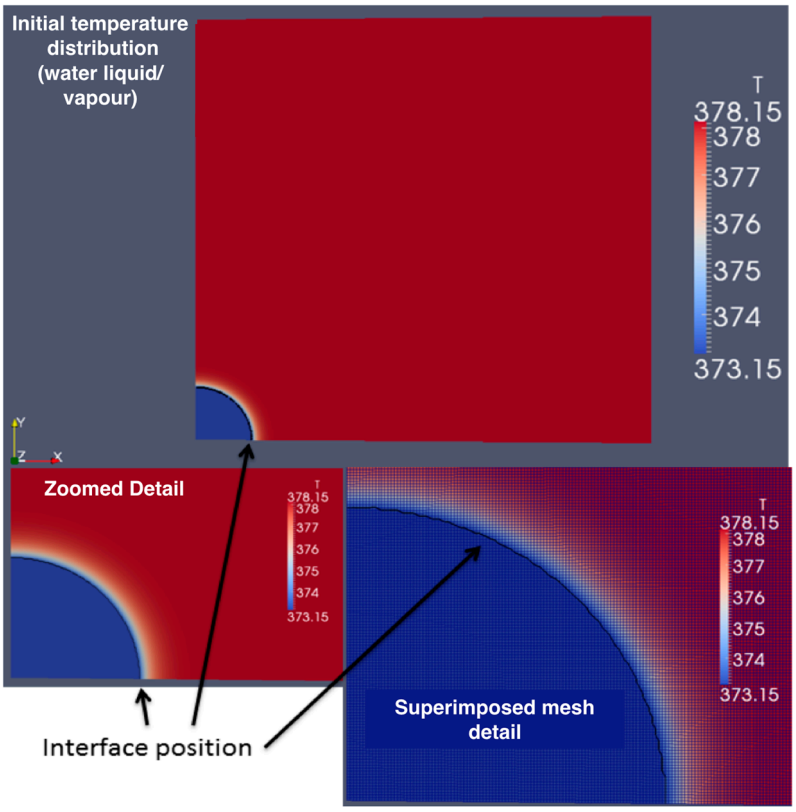

Figure 4. Initial conditions for the water liquid/vapour: P = 1.013 bar, 5 K of liquid superheat.

Table 1. Material properties and initial conditions for the numerical simulations (validation cases).

Property	Unit	Water		R134a		FC-72	
		Liquid	Vapour	Liquid	Vapour	Liquid	Vapour
Density ρ	(kg/m^3)	958	0.597	1388	4.43	1621.2	13.491
Specific heat capacity c_p	(J/kg·K)	4220	2030	1270	720	1106.7	924.81
Thermal conductivity k	(W/m·K)	0.679	0.025	0.106	0.009	0.054165	0.013778
Dynamic viscosity μ	(Pa·s)	2.77×10^{-4}	1.30×10^{-5}	4.01×10^{-4}	9.64×10^{-6}	4.13×10^{-4}	1.19×10^{-5}
Heat of vaporisation h_{lv}	(J/kg)	2,257,000		219,500		83,562	
Surface tension σ	(N/m)	0.059		0.016		0.0084	
Saturation temperature T_{sat}	(K)	373.15		303.15		330.06	
Pressure P	(bar)	1.013		0.84		1.013	
Growth constant β	(-)	14.59		8.75		7.69	
Initial thermal layer thickness δ_{therm}	m	7.00×10^{-6}		1.10×10^{-5}		1.30×10^{-5}	
Thermal diffusivity D	(m^2/s)	1.68×10^{-7}		6.01×10^{-8}		3.02×10^{-8}	
Superheat ΔT	(K)	5		5		5	

Finally, in Figure 5, the spatial and temporal evolution of the numerically predicted bubble growth is illustrated through the resulting temperature field at each time instant of the simulation for the water liquid/vapour case, while in Figure 6 a quantitative comparison of the numerical predictions with the analytical solution is conducted for all fluid cases.

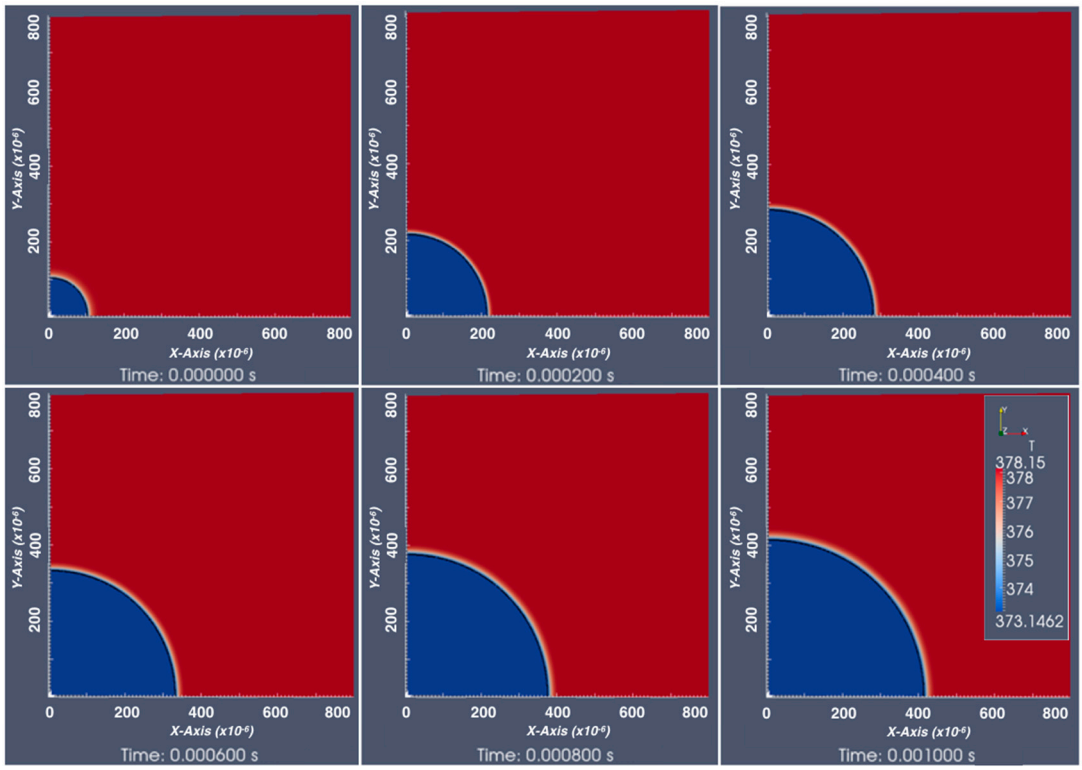

Figure 5. Bubble evolution with time for the water liquid/vapour simulation (P = 1.013 bar, ΔT = 5 K).

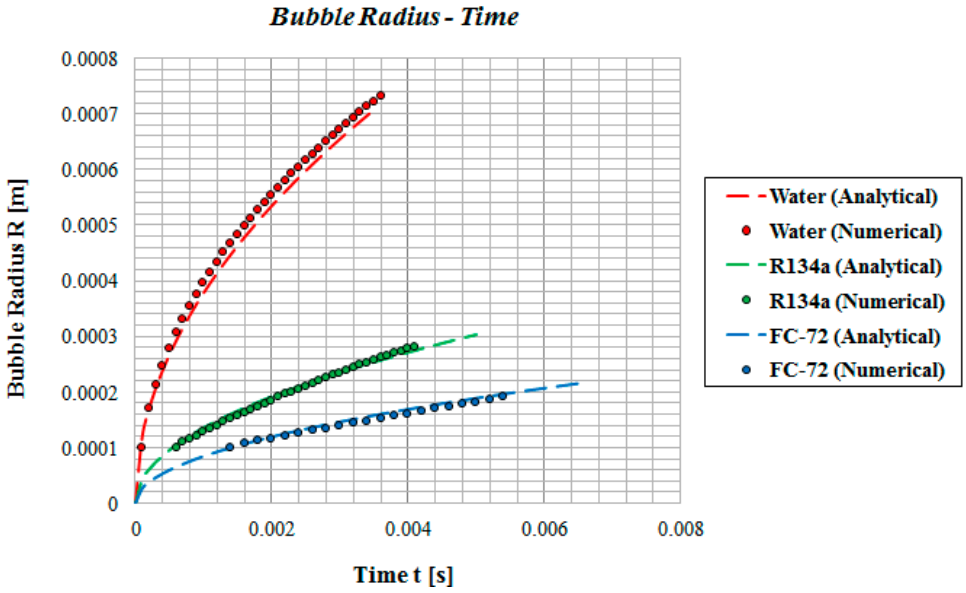

Figure 6. Bubble radius with respect to time for three different fluid cases. Comparison of numerical (present investigation) and analytical predictions [48].

As can be observed, the developed numerical model of the present paper adequately predicts the vapour bubble growth within the superheated liquid domain, for all of the considered fluid cases, in comparison with the proposed analytical solution [48].

3.2. Pool Boiling

3.2.1. Problem Definition

In order to further validate the numerical model, the experiments on single bubble growth in saturated pool boiling at a constant wall temperature boundary condition, reported in the work of Lee et al. [38], were selected, among others, since many necessary data used for their numerical reproduction are accurately reported by the authors. In more detail, in the proposed work, nucleate pool boiling experiments with constant wall temperatures were performed using R11 and R113 refrigerants, for various saturated conditions. A micro-scale heater array and Wheatstone bridge circuits were used to maintain a constant wall temperature condition and to obtain measurements with high temporal and spatial resolution. Accurate heat flow rate data were obtained from the micro-scale heater array by controlling the surface conditions at a high temporal resolution. Images of the bubble growth were captured using a high-speed CCD camera synchronised with the heat flow rate measurements. The geometry of the bubble was obtained from the images. In the present paper, one specific experimental run for R113 is reproduced numerically and presented as a validation case.

3.2.2. Computational Set-Up

Since, the processes of bubble growth and detachment in the proposed experiment can be considered to be axisymmetric, an axisymmetric computational domain was constructed for its numerical reproduction. The adopted computational domain, mesh and boundary conditions are illustrated in Figure 7. As can be seen, a wedge-type geometry was constructed, representing a 5° section of the corresponding 3D domain in the considered physical problem. A non-uniform structured computational mesh with local refinement was used, consisting of 400,000 hexahedral cells. A minimum cell size of 2 μm and a maximum cell size of 4 μm were selected in the bottom left and top right corners of the computational domain, respectively, in order for the solution to be mesh-independent. The overall domain size in the XY plane is 2.5 mm × 4 mm. These dimensions were indicated from initial trial simulations that were conducted in order to determine the minimum distances between the axis of symmetry and the side wall boundary (domain width), as well as between the bottom wall and the outlet (domain height), in order to avoid any influence of these boundaries in the computed bubble growth and detachment process.

At the solid walls, a no-slip velocity boundary condition was used with a fixed flux pressure boundary condition for the pressure values. At the lower wall, a constant contact angle of $\theta = 30^\circ$ was imposed for the volume fraction field. According to Lee et al. [38], the static equilibrium contact angle of the micro-scale heater array surface was 11.4° for R113. However, the dynamic characteristics of a boiling bubble are supposed to be different with respect to the static equilibrium contact angle, which is usually measured with the sessile drop method, and at ambient temperature and pressure conditions. Therefore, the value of $\theta = 30^\circ$ which was finally selected for the numerical simulation was chosen after a series of parametric numerical simulations, where contact angles ranging from 11.4° to 160° were tested. The adopted value of $\theta = 30^\circ$ indicated the closest numerical predictions to the corresponding experimental observations. The proposed parametric analysis is presented in detail in Section 4.2. For the side wall, a zero-gradient boundary condition was used for the volume fraction values. As for the temperature field, a constant temperature of $T_w = 334.15$ K (in accordance with the selected experimental run) was imposed in the bottom wall and a zero-gradient boundary condition was used for the sidewall. At the outlet, a fixed-valued pressure boundary condition and a zero-gradient boundary condition for the volume fraction were used, while for the velocity values, a special (combined) type of boundary condition was used that applies a zero gradient when the fluid mixture exits the computational domain and a fixed-value condition to the tangential velocity component, in cases where fluid enters the domain. Finally, a zero-gradient boundary condition for the temperature field was also prescribed at the outlet boundary. The fluid properties for the initial

conditions as well as some computational details for the simulation imitating the selected experimental run are summarised in Table 2.

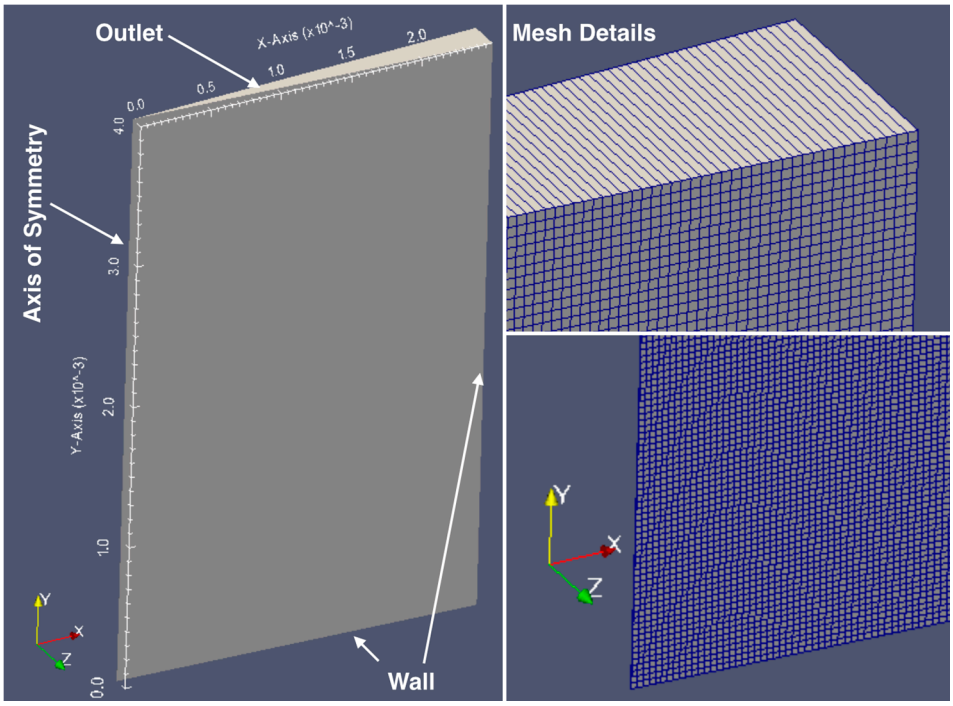

Figure 7. Computational domain, mesh and boundary conditions.

Table 2. Fluid properties and initial conditions.

		ρ (kg/m^3)	c_p (J/kgK)	k (W/mK)	ν (m^2/s)	σ (N/m)	h_{lv} (J/kg)
Phase properties (R113 at 1 bar, T_{sat} = 320.65 K)	Liquid	1508.4	940.3	0.064	3.25×10^{-7}	0.015	144,350
	Vapour	7.4	691.3	0.0095	1.39×10^{-6}		
Initial Conditions	Initial bubble (seed) radius: 50 µm		ΔT = 13.5 K Contact angle: 30°		Domain size (mm): 2.5 × 4.0		
	Initially developed thermal boundary layer thickness: 352 µm		Simulation Type: axisymmetric		No. of computational cells: 400,000		

The initial temperature of the R113 liquid in the computational domain was assumed to be at saturation temperature. Then a single-phase transient solution was started for a certain time period in order for the initial temperature boundary layer to be developed in the vicinity of the heated wall. After the development of a desired temperature boundary layer thickness, an initial seed bubble with a radius of 50 µm was patched at the bottom wall, as a 5° section of a hemisphere (axisymmetric simulation), which immediately started to evaporate. The initial condition for the two-phase simulation corresponded to the time when the bubble seed was planted in the domain (Figure 8).

At this point it should be mentioned that, since the initial thermal boundary layer thickness was not measured in the experiments of Lee et al. [38], a series of parametric numerical simulations were performed, utilising a wide number of successive thicknesses, developed in the single-phase simulation at successive time instances. More details regarding the effect of the initially developed boundary layer characteristics on the bubble growth and detachment process are given in Section 4.1. A thickness of 352 µm, which corresponds to a development time of 0.08 s, showed the best match with the corresponding experimental results.

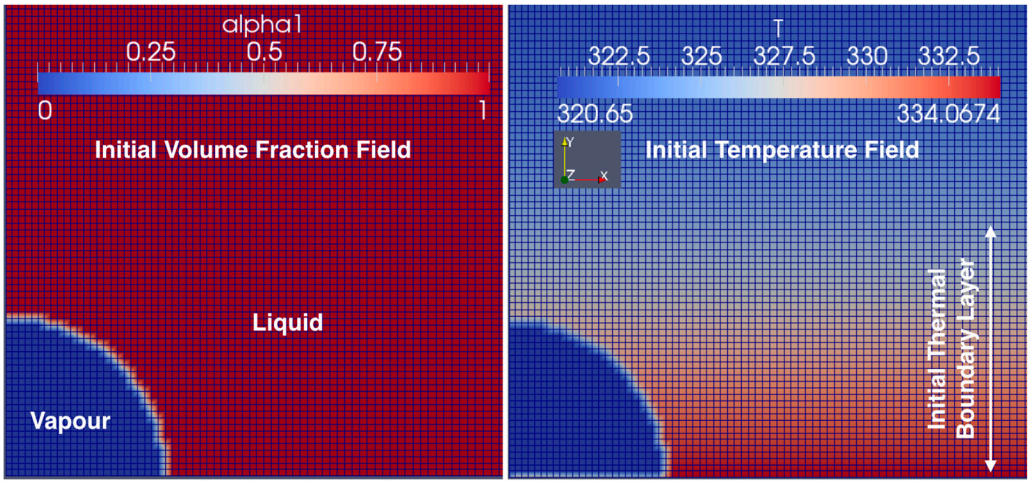

Figure 8. Initial conditions for the simulation.

3.2.3. Comparison of Numerical and Experimental Results

In Figure 9, the reconstructed 3D evolution of the 0.5 volume fraction contour (interface) from the axisymmetric simulation is compared with the corresponding experimental snapshots for approximately the same time instances that correspond to the bubble detachment stage, while in Table 3 the numerically predicted bubble detachment characteristics are compared with the corresponding experimental values.

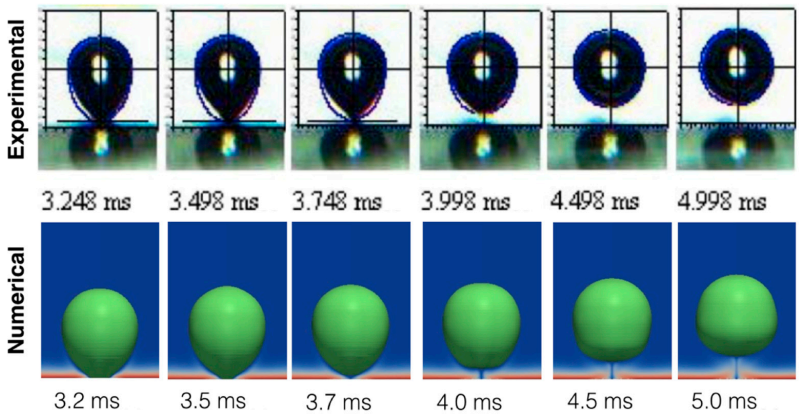

Figure 9. Qualitative comparison of experimental [38] and numerical (present investigation) 3D bubble evolution.

Table 3. Predicted (present investigation) and measured [38], bubble detachment characteristics.

	Bubble Detachment Time (ms)	Equivalent Bubble Detachment Diameter (mm)
Experimental [38]	3.748	0.704
Numerical (present investigation)	3.700	0.740
% Error	1.28	5.11

As can be observed, the numerical model predictions are in very good agreement with the corresponding experimental data. The numerically predicted spatial and temporal evolution of the generated bubble matches very well with the corresponding experimental images (Figure 9). Some small deviations in the shape of the bubble, especially after its detachment from the heated plate, can be attributed to the fact that the proposed experimental images were recorded after a few bubble

cycles, while the numerical simulation images represent the first bubble cycle. However, as is indicated in Table 3, the numerical model predictions regarding the bubble detachment time and the equivalent bubble detachment diameter are in very close agreement with the corresponding experimental values.

4. Application of the Validated Numerical Model for the Simulation of Pool Boiling Characteristics

In the current section of the present work, the validated numerical model is further applied for the conduction of four different series of parametric numerical simulations, aiming to identify and quantify the effects of fundamental controlling parameters in the bubble growth and detachment characteristics, identified as being important during the validation process.

In more detail, the first series (Series A) aims to identify the effect of the initial thermal boundary layer, the second (Series B) the effect of the triple-line contact angle (wettability), the third (Series C) the effect of the wall superheat and the fourth (Series D) the effect of the gravity level in the bubble growth and detachment characteristics.

In all these simulations, the same computational domain, mesh and boundary conditions with the validation case presented in the previous section were used. Three different refrigerants were used as working fluids. R113, as in the validation section of the present paper, was used for Series A, while R113 as well as R22 and R134a were used for the numerical simulations of Series B, C and D, since these are among the most widely used working fluids in boiling applications. The corresponding fluid properties and initial conditions for the base cases, which are used as a reference in the proposed series of parametric numerical simulations, are summarised in Appendix A, Tables A1–A3, respectively.

The temporal and spatial evolution of the bubble growth and detachment process for the base case of Table A1 (Appendix A) is depicted indicatively in Figure 10, where the interface position between the vapour and liquid phases (green surface) is illustrated for successive time instances, from the 3D reconstruction of the axisymmetric simulation results.

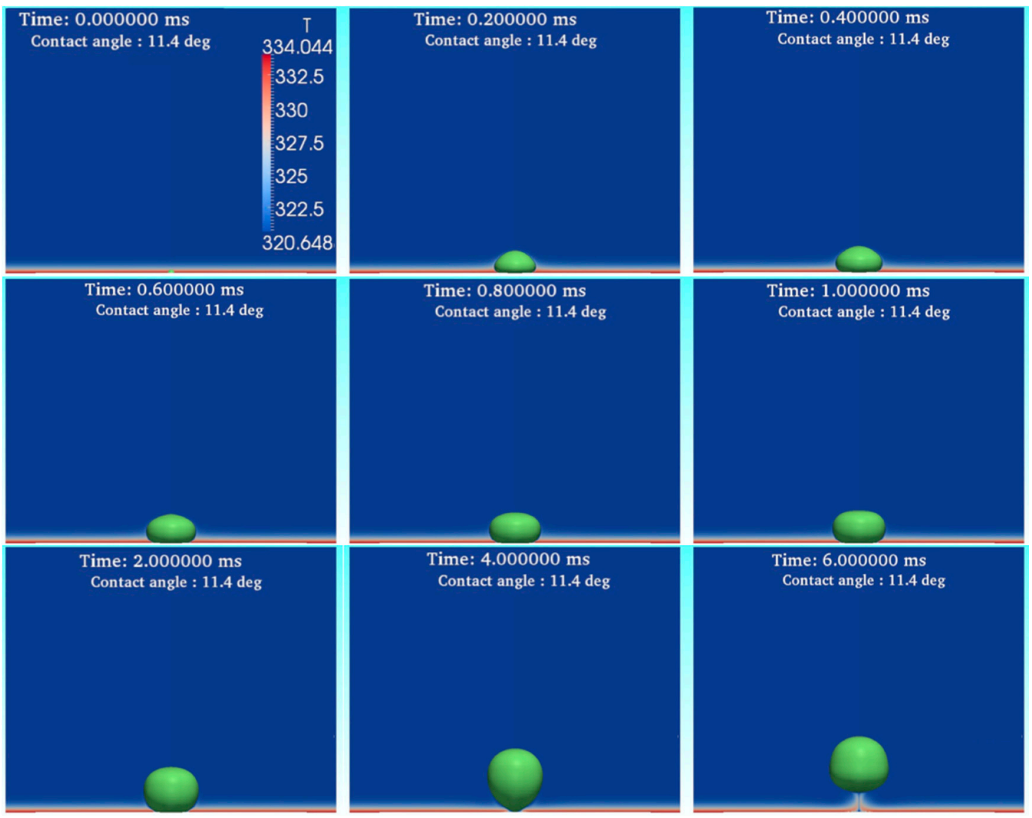

Figure 10. Three-dimensional bubble spatial and temporal evolution (base case, R113).

As can be observed, the initially seeded bubble nucleus (t = 0 ms) grows and finally detaches from the superheated wall. As was expected, initially, the bubble base diameter increases since the evaporating meniscus on the bubble foot slides outwards up to a certain point, and finally decreases, sliding inwards up to the instance of detachment. After detachment from the heated wall, the bubble rises in the liquid domain due to buoyancy. Furthermore, a characteristic depletion of the thermal boundary layer is observed after the bubble detachment, while the rising bubble carries some heat upwards in its tail. These qualitative observations are in agreement with previous similar investigations (e.g., [23,49,50]).

4.1. Effect of Initial Thermal Boundary Layer—Series A

Since the superheated bulk liquid thermal boundary layer thickness determines how much heat is stored in the fluid layer in the vicinity of the heated plate, it was deemed appropriate for a parametric study to be conducted, aiming to identify the effect of the initial thermal boundary layer (ITBL) thickness, on the bubble growth and detachment process. Therefore, in the current section of the present paper, the effect of the ITBL on the bubble detachment characteristics is investigated numerically. For this purpose, the base case of Table 4 is utilised and additional simulations are performed by systematically varying the ITBL that is imposed, as an initial condition, in the vicinity of the heated plate (bottom wall boundary of the computational domain). In more detail, a single-phase transient simulation is first performed and the developed thermal boundary layers are extracted in certain successive time steps. These are then used as the initial condition for the temperature field in the two-phase numerical simulations that comprise the proposed parametric analysis (Series A numerical simulations). All the other simulation parameters are kept constant with respect to the base simulation case (Table A1). Details regarding the overall runs conducted are summarised in Table 4.

Table 4. Varied parameters in Series A of parametric numerical simulations.

Run	Time of ITBL Development (Single-Phase Simulation) (s)	Thickness of ITBL (μm)
A1	0.01	136
A2	0.02	184
A3	0.03	216
A4	0.06	304
A5	0.07	328
A6 (base case, R113)	0.08	352
A7	0.09	376
A8	0.1	392
A9	0.2	552
A10	0.3	680

As can be observed, a total number of nine additional simulations were performed, changing the initial temperature field in each case. The reference/base case in Table 4 corresponds to the validation run of Figure 9. The prescribed ITBL in each case is illustrated diagrammatically in Figure 11, where the initial variation of temperature with respect to the vertical distance from the heated plate is plotted for each run of Series A numerical simulations.

The spatial evolution of the generated bubbles for each of the above cases at the time of detachment is depicted in Figure 12. As can be observed, there was a substantial increase in the bubble growth and detachment characteristics with respect to the corresponding increase in the thickness of the ITBL. The thicker the ITBL, the bigger the bubble diameter at detachment. These findings are in direct qualitative agreement with previous similar investigations (e.g., [51]).

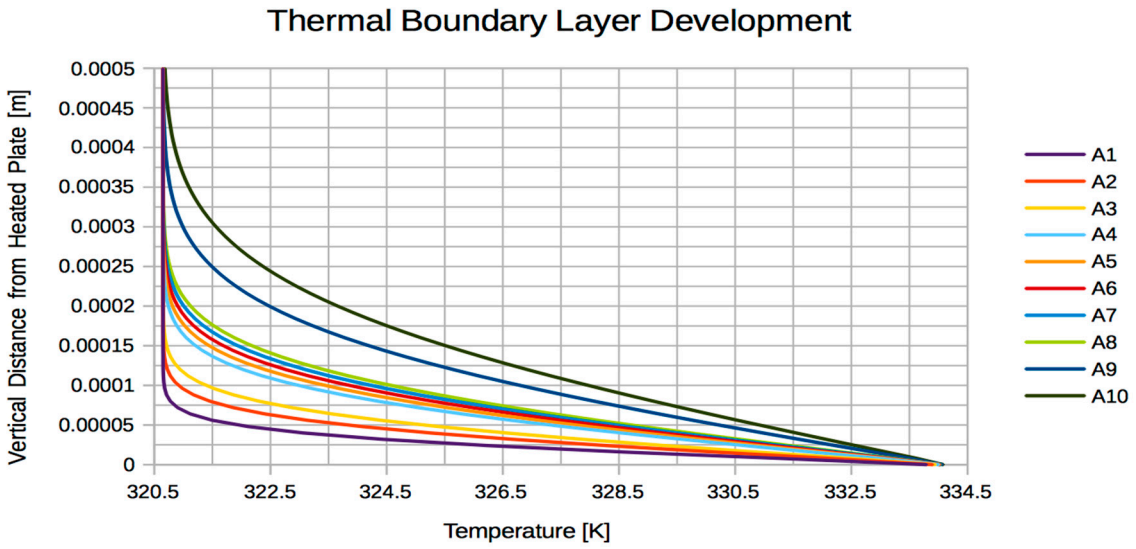

Figure 11. ITBL for each run of the Series A parametric numerical simulations.

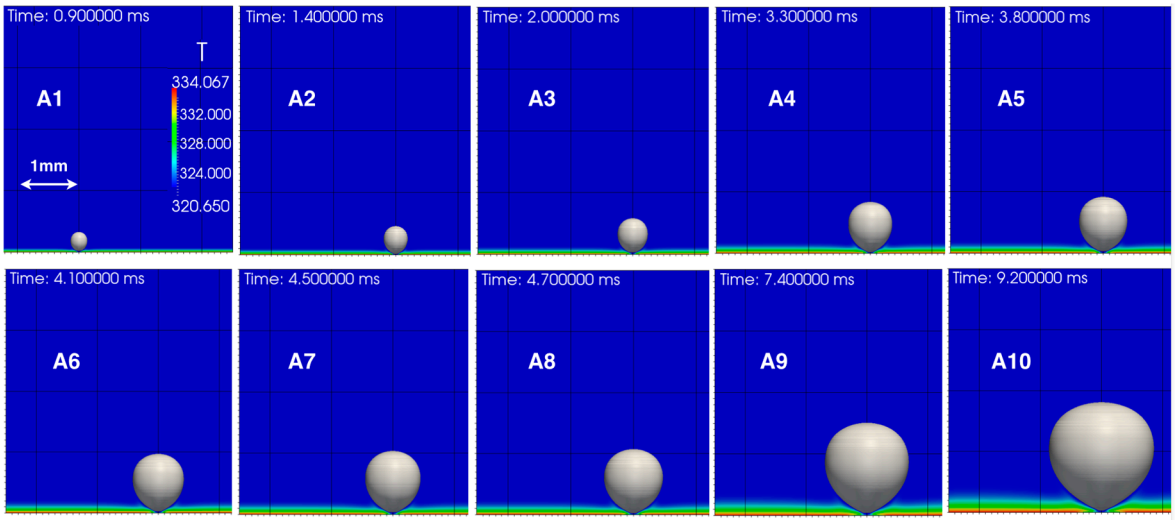

Figure 12. Spatial evolution of generated bubble at the time of detachment for each case of Series A.

The bubble detachment time with respect to the ITBL thickness is plotted in Figure 13a, while the equivalent bubble detachment diameter with respect to the ITBL thickness is plotted in Figure 13b. It should be mentioned here that the diameter of a sphere, having the same volume as the corresponding bubble in each case at the time of detachment from the heated plate, is taken as the equivalent bubble detachment diameter.

As can be observed, the increase of the ITBL causes a linear increase in both the bubble detachment time as well as the equivalent bubble detachment diameter. It is characteristic that an increase of the ITBL by a factor of five causes a corresponding increase in the bubble detachment time and the equivalent bubble detachment diameter by a factor of nine and six, respectively. From all the above, it is evident that the ITBL is a very influential and important parameter in the bubble growth and detachment process. Therefore, it is strongly suggested that the bulk liquid thermal boundary layer thickness should be measured and reported in future experimental studies, since it comprises a required input for the successful numerical simulation of nucleate boiling processes. According to the authors' best knowledge, this is the first time that this effect has been examined, identified and quantified in detail.

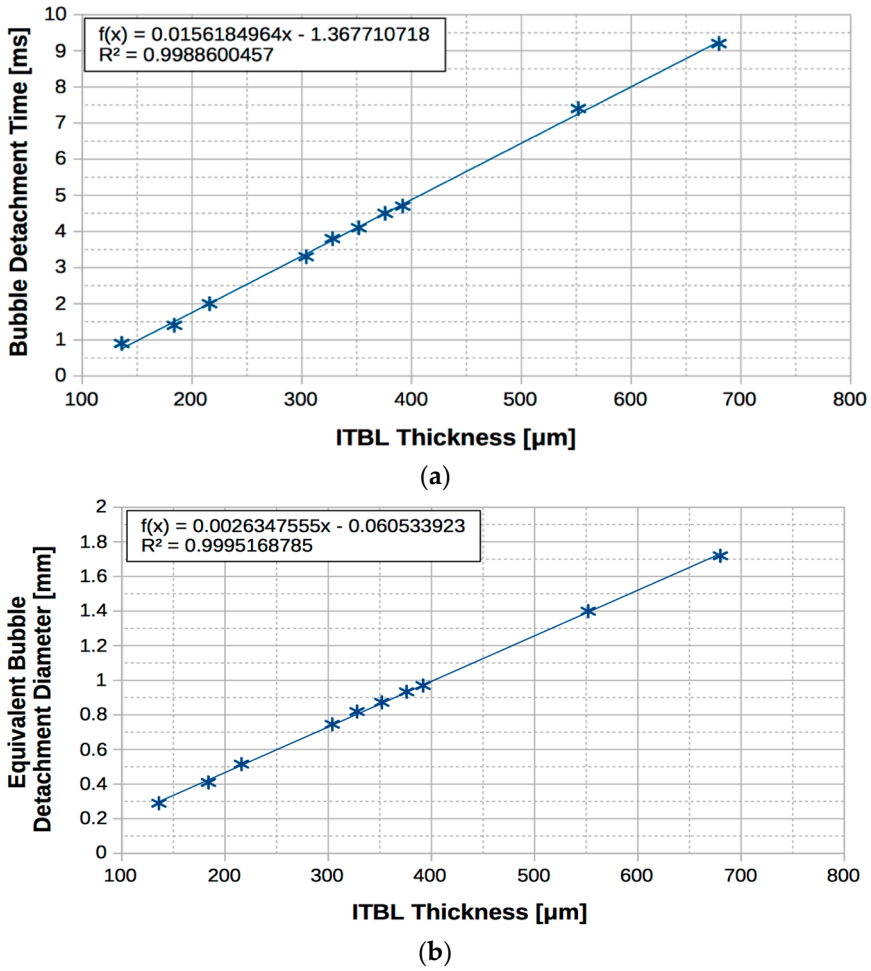

Figure 13. Effect of ITBL thickness on: (**a**) the bubble detachment time; (**b**) the equivalent bubble detachment diameter.

4.2. Effect of Surface Wettability—Series B

Past studies have identified surface wettability as one of the most important factors affecting bubble nucleation, growth and detachment (e.g., [27,52–54]) and they provide a good summary of the current understanding. The effect of surface wettability on bubble growth can be incorporated in a numerical model by the imposed contact angle between the vapour/liquid interface and the heated solid surface (triple-line). In the current section of the present paper, the effect of wettability on the bubble detachment characteristics is investigated numerically. For this purpose, the base cases of Tables 4–6 are utilised and additional simulations are performed by systematically varying the value of the triple-line (solid–liquid–vapour) contact angle at the bottom wall boundary of the computational domain. All the other simulation parameters are kept constant with respect to the base simulation cases (Tables A1–A3 in Appendix A). Details regarding the overall runs are summarised in Table 5.

Table 5. Varied parameters in Series B of parametric numerical simulations.

Run	Contact Angle (°)	Working Fluid	Run	Contact Angle (°)	Working Fluid	Run	Contact Angle (°)	Working Fluid
B1 (Base Case R113)	11.4	R113	B16	15	R22	B31	15	R134a
B2	15	R113	B17	20	R22	B32	20	R134a
B3	20	R113	B18	25	R22	B33	25	R134a
B4	25	R113	B19 (base case, R22)	30	R22	B34 (base case, R134a)	30	R134a
B5	30	R113	B20	35	R22	B35	35	R134a
B6	35	R113	B21	40	R22	B36	40	R134a
B7	40	R113	B22	45	R22	B37	45	R134a
B8	45	R113	B23	50	R22	B38	50	R134a
B9	50	R113	B24	55	R22	B39	55	R134a
B10	55	R113	B25	60	R22	B40	60	R134a
B11	60	R113	B26	65	R22	B41	65	R134a
B12	65	R113	B27	70	R22	B42	70	R134a
B13	70	R113	B28	75	R22	B43	75	R134a
B14	75	R113	B29	80	R22	B44	80	R134a
B15	80	R113	B30	85	R22	B45	85	R134a

As can be seen, a total of 45 simulations were performed, varying the imposed contact angle at the bottom wall boundary from 11.4° up to 80° for the cases of R113 runs (B1 to B15) and from 15° to 85° for the cases of R22 (B16 to B30) and R134a (B31 to B45) runs. The spatial evolution of the generated bubbles for each of the above cases, at the time of detachment, is depicted in Figures 14–16, for the R113, R22 and R134a cases, respectively.

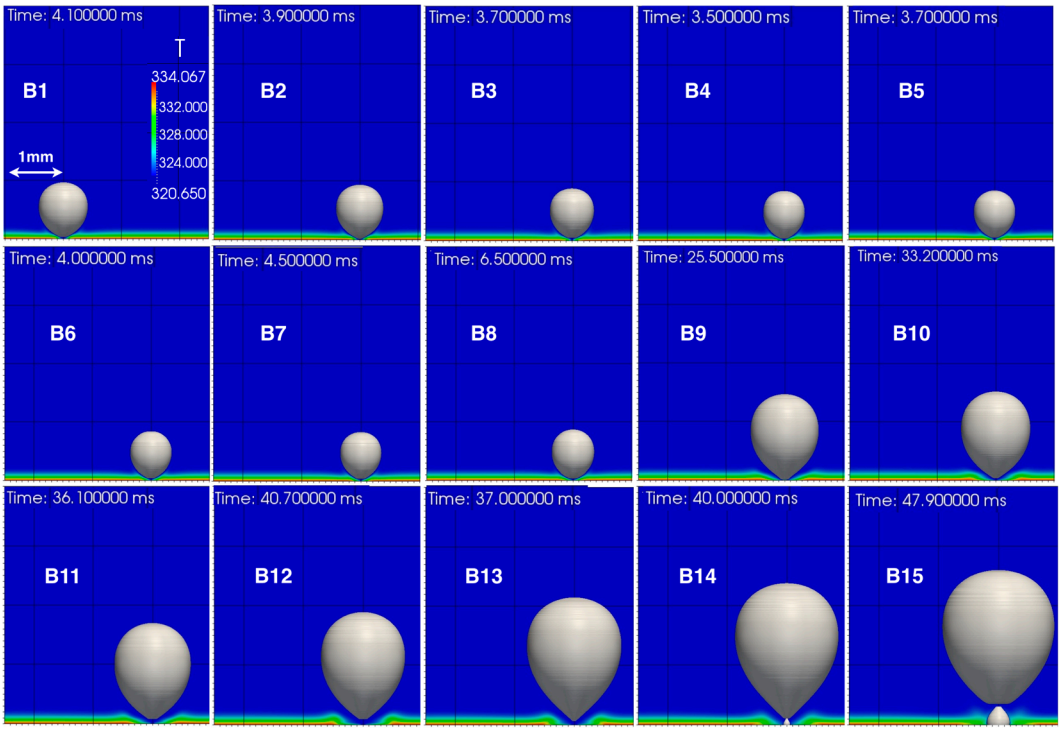

Figure 14. Spatial evolution of generated bubble at the time of detachment for each R113 case of the Series B parametric numerical simulations.

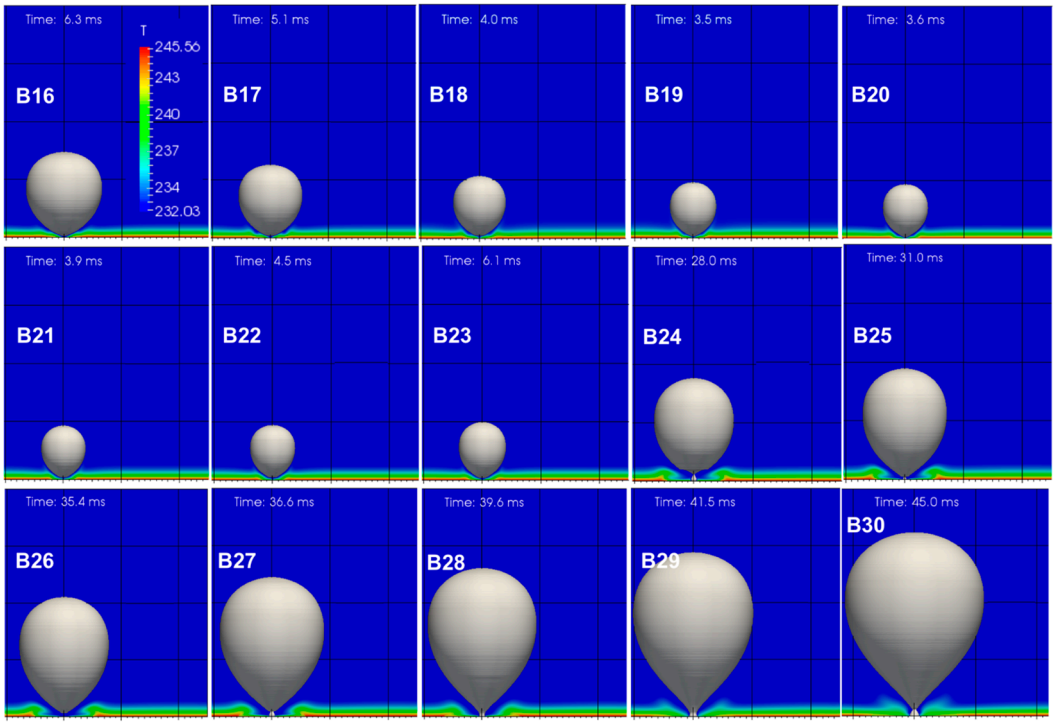

Figure 15. Spatial evolution of generated bubble at the time of detachment for each case R22 of the Series B parametric numerical simulations.

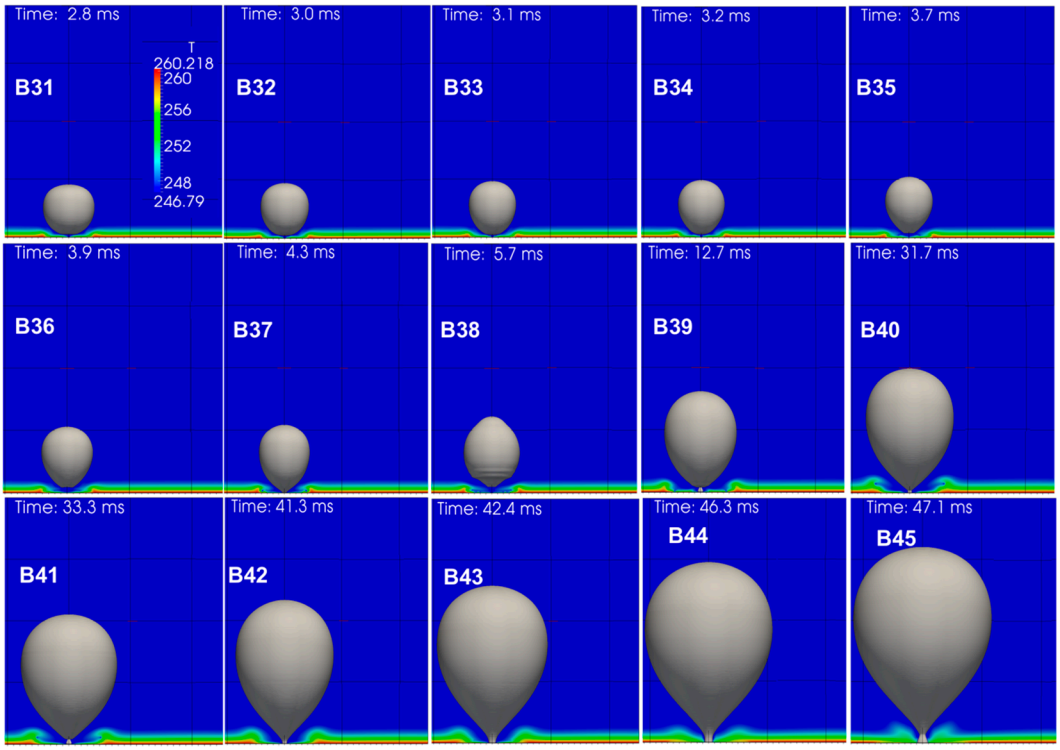

Figure 16. Spatial evolution of generated bubble at the time of detachment for each R134a case of the Series B parametric numerical simulations.

As can be observed from Figure 14, for the R113 runs, initially the successive increase of the imposed contact angle from 11.4° (case B1) up to 45° (case B8) had a relatively minimal effect on the

bubble detachment characteristics. On the other hand, for equilibrium contact angles greater than 45° (cases B9 to B15), the effect of the contact angle on both the bubble detachment volume and the bubble detachment time appeared to be more significant. In more detail, the bubble detachment volume slightly decreased (cases B2 and B3) and then remained almost constant (cases B4–B8). However, a slightly different effect could be observed in the predicted bubble detachment times. The bubble detachment time initially showed a small decrease (cases B2–B4), and then it successively started to show a small increase again (cases B5–B8). When the imposed contact angle successively increased above 45° (cases B9–B15), it caused a subsequent increase in the bubble detachment volume. Approximately the same trend could be observed also for the bubble detachment time.

However, it is characteristic that while the bubble detachment time continuously increased with the corresponding increase in the contact angle (cases B9–B12), at a certain point (cases B13 and B14) it remained almost constant and then continued to increase (case B15).

Another interesting observation is the fact that for contact angles greater than 70° (cases B14 and B15), the bubble departed from the heated surface, leaving behind a small residual bubble nucleus on the surface.

For the R113 runs (Figure 15), the successive increase of the imposed contact angle from 15° up to 45° (cases B16–B22) had a relatively small effect on the bubble detachment characteristics. However, as in the case of the R113 runs, there was a significantly greater effect of the contact angle increase on both the bubble detachment time and volume for contact angles greater than 45°. In more detail, there was a small successive decrease in the bubble detachment volume as the contact angle increased from 15° to 30° (cases B16–B19) and then it remained constant from 35° to 45° (cases B20–B22). For angles greater than 45°, the successive increase of the contact angle caused a significant increase in the bubble detachment volume (B23–B30). A similar behaviour could also be observed for the bubble detachment time.

Finally, for the R134a runs (Figure 16), an almost negligible effect of the contact angle increase on both the bubble detachment time and bubble detachment volume could be observed for contact angles lower than 45°, while a significant increase in the bubble detachment characteristics was evident with the corresponding increase of the imposed contact angle for values greater than 45°.

As can also be confirmed by the diagrams of Figure 17, the bubble detachment characteristics seemed to be significantly affected by the imposed contact angle, i.e., the wettability of the heated plate, with values higher than 45° showing an irregular increase. However, the proposed effect was minimal for contact angles lower than this limiting value of 45°. It is important to note that in total, for each of the considered working fluids, increasing the contact angle by an approximate factor of eight caused a significant increase in the bubble detachment time by a factor of 10, while the equivalent bubble detachment diameter increased by a smaller but still significant factor of approximately three.

Therefore, it is evident that two distinct behavioural regions can be identified in the diagrams of Figure 17 which are common for all three examined working fluids: a "lyophilic" region ($\theta \leq 45°$) without significant changes in the bubble detachment characteristics and a "lyophobic" region ($\theta > 45°$) where both the bubble detachment time and the equivalent bubble detachment diameter are highly affected by the wettability of the heated plate. According to the authors' best knowledge, there are not, at the moment, any experimental or numerical demonstrations of this phenomenon.

Cases with even higher contact angles were also tested for the case of R113 (up to a value of 160°). For this purpose, a bigger computational domain was constructed (5 mm × 8 mm), keeping the same computational mesh characteristics as the ones described in Section 3.2.2. Some indicative results are depicted in Figure 18, where the spatial evolution of the generated bubbles after approximately 50 ms from the nucleation time is depicted for four different cases with corresponding contact angle values of 90°, 115°, 130° and 140°, respectively.

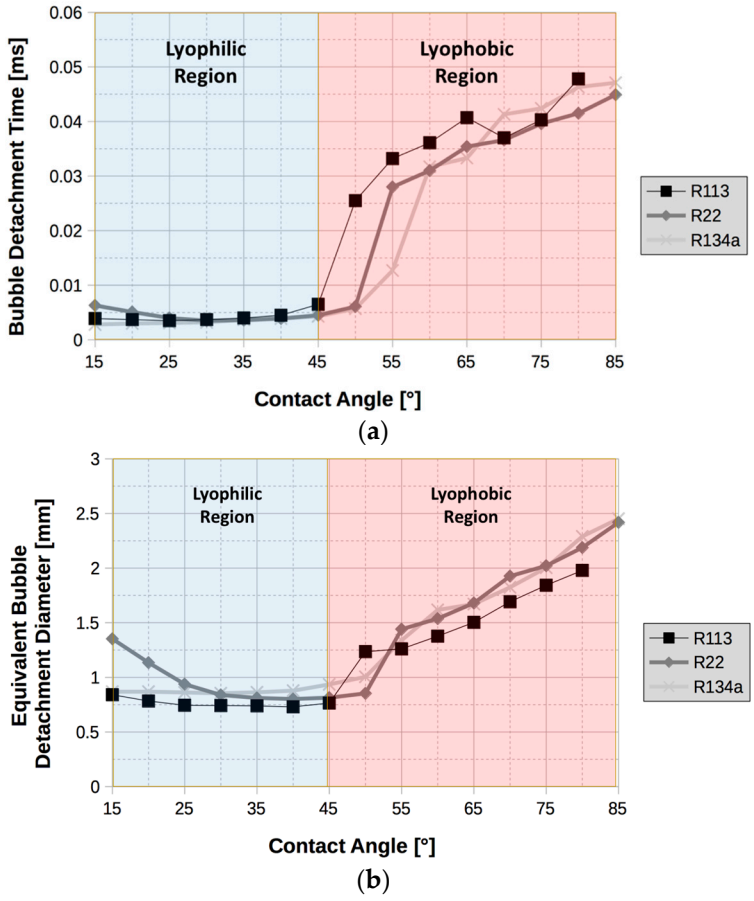

Figure 17. Effect of contact angle on: (**a**) the bubble detachment time; (**b**) the equivalent bubble detachment diameter.

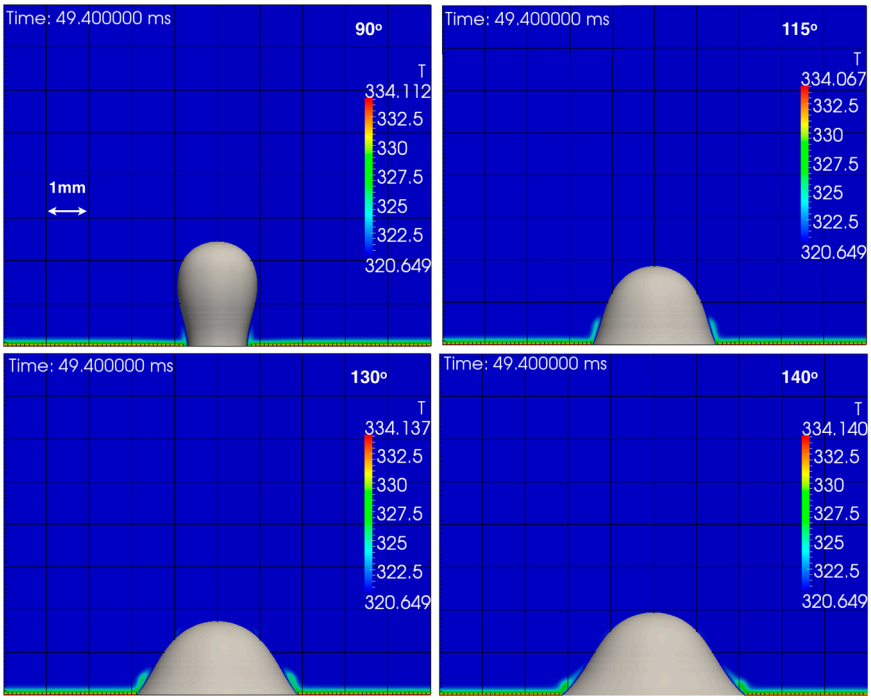

Figure 18. Evolution of a R113 bubble, at t = 49.40 ms, for equilibrium contact angles higher than 80°.

As can be observed, as the contact angle increased beyond the value of 80°, the bubble detachment time subsequently increased significantly; especially after reaching a contact angle of 100°, the bubble continuously grew and its initial meniscus continuously slid outwards, tending to form a vapour film. This observation is in direct qualitative agreement with previous investigations of pool boiling of water on hydrophilic, hydrophobic and super-hydrophobic surfaces (e.g., [55,56]). An example on the generated bubble before detachment for a hydrophilic (contact angle of 30°) and a hydrophobic (contact angle of 150°) surface, from the work of Malavasi et al. [56], is given in the experimental snapshots of Figure 19.

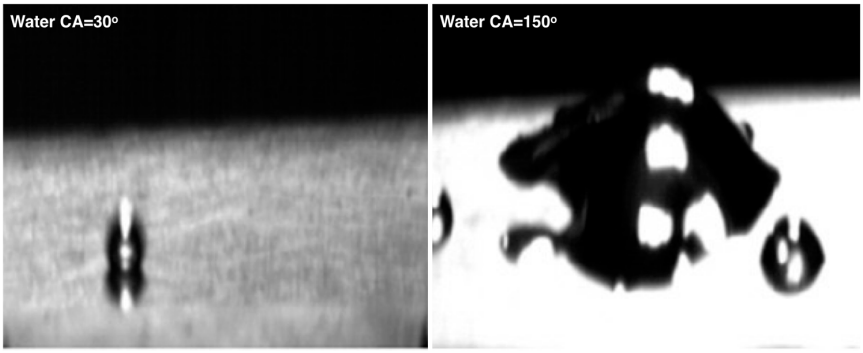

Figure 19. Experimental images of pool boiling of water on hydrophilic and hydrophobic surfaces [56].

As can be seen, in the case of the hydrophilic surface, the shape of the bubble before its detachment is closer to case B4 of the present investigation (Figure 14), while the case of the hydrophobic surface is in close qualitative agreement with the case of 140° of Figure 18.

All the above findings indicate that the wettability of the heated surface in nucleate boiling is another quite important factor that significantly affects the bubble growth and detachment characteristics.

4.3. Effect of Wall Superheat—Series C

In the current section of the present paper, the effect of the wall superheat on the bubble detachment characteristics is investigated numerically. For this purpose, the base cases of Tables A1–A3 (Appendix A) are utilised and additional simulations are performed by systematically varying the value of the heated plate superheat (bottom wall boundary of the computational domain). All the other simulation parameters are kept constant with respect to the base simulation cases. Details regarding the overall runs conducted are summarised in Table 6.

Table 6. Varied parameters in Series C of parametric numerical simulations.

Run	Wall Superheat (K)	Working Fluid	Run	Wall Superheat (K)	Working Fluid
C1	5.5	R113	C16	17.5	R22
C2	10.5	R113	C17	18.5	R22
C3 (base case, R113)	13.5	R113	C18	19.5	R22
C4	14.5	R113	C19	2.5	R134a
C5	15.5	R113	C20	5.5	R134a
C6	16.5	R113	C21	10.5	R134a
C7	17.5	R113	C22 (base case R134a)	13.5	R134a
C8	18.5	R113	C23	14.5	R134a
C9	19.5	R113	C24	16.5	R134a
C10	2.5	R22	C25	17.5	R134a
C11	5.5	R22	C26	18.5	R134a
C12	10.5	R22	C27	19.5	R134a
C13 (base case R22)	13.5	R22			
C14	14.5	R22			
C15	16.5	R22			

As can be seen, a total of 27 simulations were performed, varying the bottom wall superheat from 5.5 K up to 19.5 K for the R113 runs and from 2.5 K up to 19.5 K for the R22 and R134a runs, respectively. It should be mentioned here that as for the validation case (C3), a single-phase transient numerical simulation was initially performed in each of the above cases and the developed ITBL at 0.08 s was used as the initial condition for the temperature field in the two-phase simulations. This was done in order to start each case with approximately the same thickness of the ITBL but with a different superheat. The spatial evolution of the generated bubbles for each of the above cases, at the time of detachment, is depicted in Figures 20–22 for the R113, R22 and R134a runs, respectively.

As can be observed, both the bubble detachment time as well as the bubble detachment volume were highly sensitive to the wall superheat. In more detail, a successive increase in the bottom wall superheat caused a quite considerable subsequent increase in the bubble detachment characteristics. However, in order to quantify the exact influence of the wall superheat on the bubble detachment characteristics, the diagrams of Figure 23 are plotted. In more detail, the bubble detachment time with respect to the applied wall superheat is plotted in Figure 23a, while the equivalent bubble detachment diameter is plotted in Figure 23b.

As can be observed, the increase of the applied wall superheat caused a subsequent increase in both the bubble detachment time as well as the equivalent bubble detachment diameter, following a power law, for all three of the examined working fluids. It is characteristic that an increase in the applied superheat by a factor of just 3.5 caused a corresponding increase in the bubble detachment time and the equivalent bubble detachment diameter by an approximate factor of 18 and 10 for R113 and nine and six for R22 and R134a, respectively. All these findings and observations are in direct qualitative agreement with previous similar investigations (e.g., [57]).

As expected, the value of the heated wall superheat is a very important parameter in the bubble growth and detachment process. Even a temperature variation of a few degrees can significantly alter the bubble detachment characteristics. Therefore, it can be concluded that the accurate measurement of the temperature values in the vicinity of the generated bubbles is quite crucial for the numerical reproduction of experimental results on nucleate boiling.

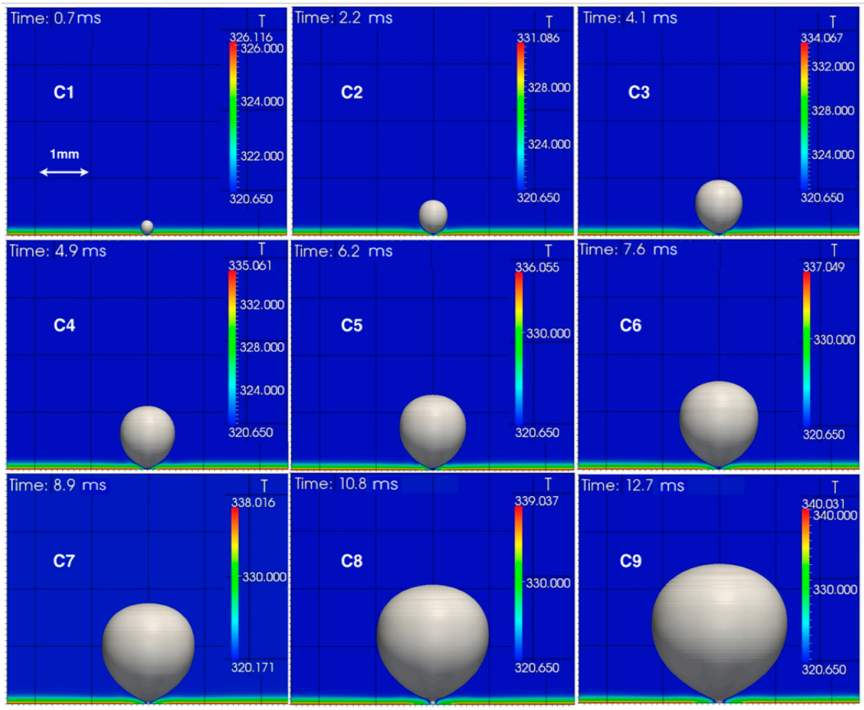

Figure 20. Spatial evolution of generated bubble at the time of detachment for each R113 case of the Series C parametric numerical simulations.

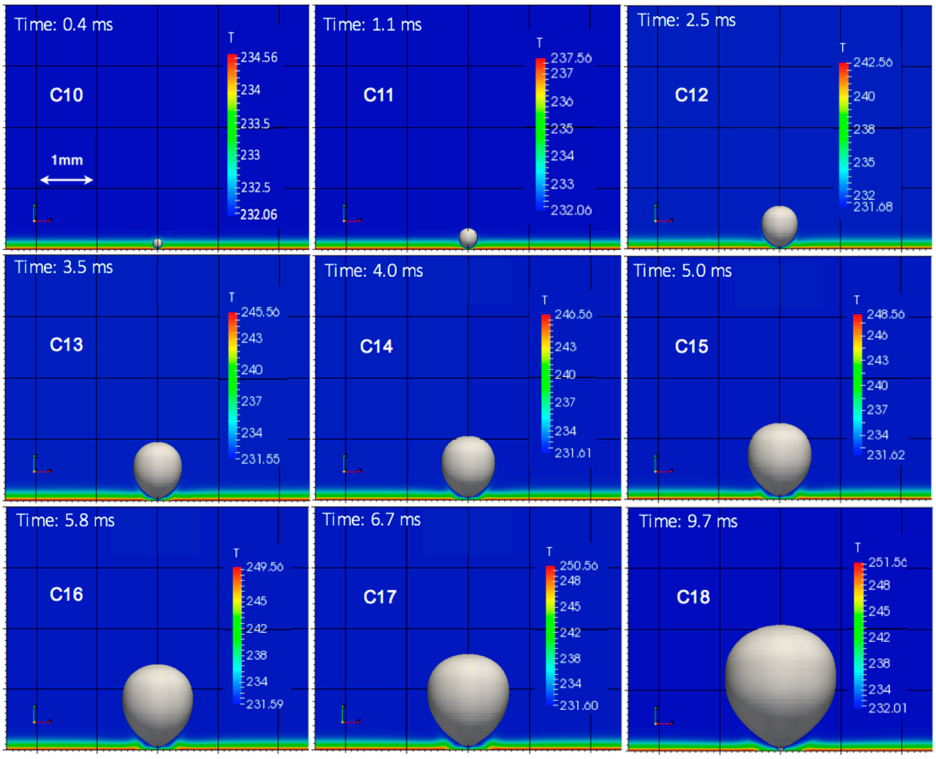

Figure 21. Spatial evolution of generated bubble at the time of detachment for each R22 case of the Series C parametric numerical simulations.

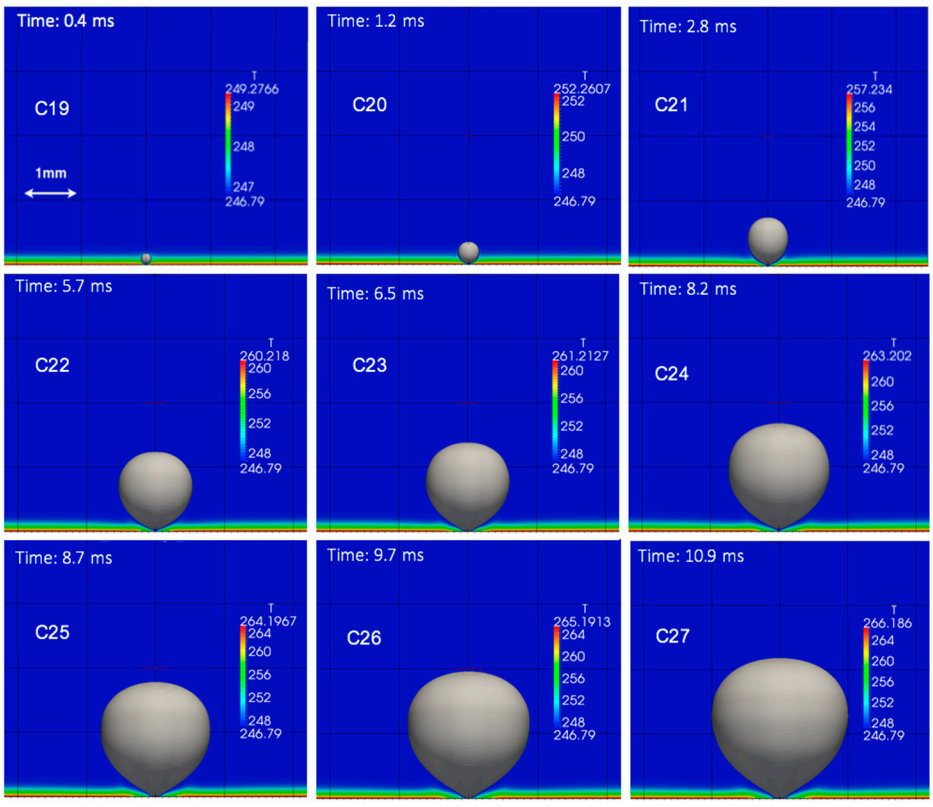

Figure 22. Spatial evolution of generated bubble at the time of detachment for each R134a case of the Series C parametric numerical simulations.

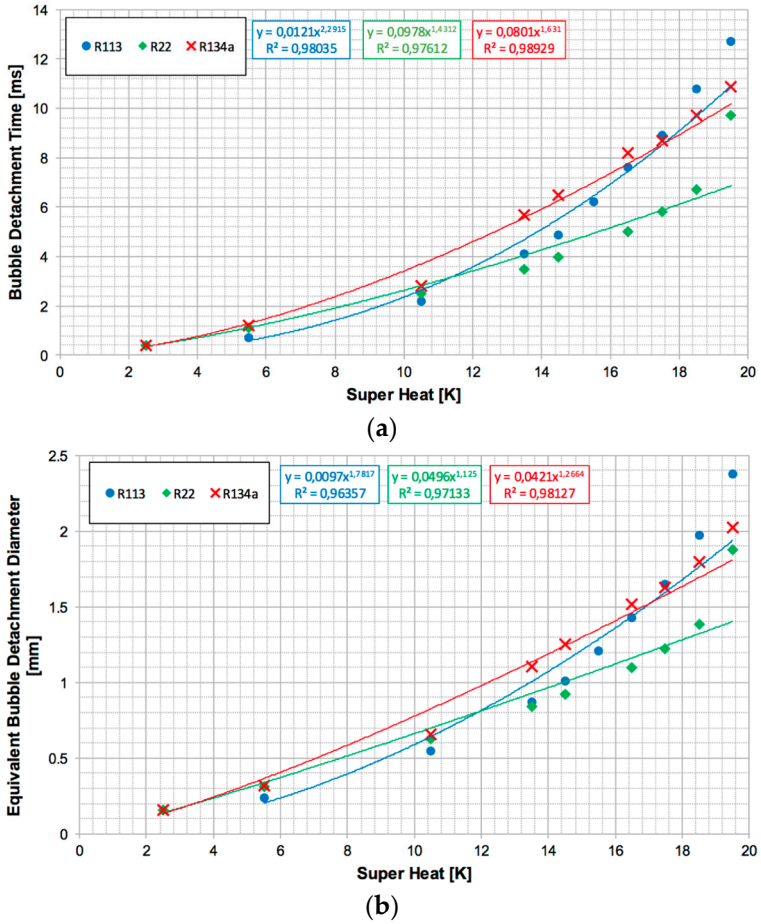

Figure 23. Effect of wall superheat on (**a**) the bubble detachment time; and (**b**) the equivalent bubble detachment diameter.

4.4. Effect of Gravity Level—Series D

In the current section of the present paper, the effect of the gravity level on the bubble detachment characteristics is investigated numerically. For this purpose, the base cases of Tables A1–A3 (Appendix A) are utilised and additional simulations are performed by systematically varying the value of the gravitational acceleration. Five different gravity levels that correspond to the gravitational acceleration values of all the major planets in the Earth's solar system are utilised for the proposed parametric analysis. It must be mentioned that the proposed analysis is again performed for the same working fluids (R113, R22 and R134a), not only for atmospheric pressure conditions (1 bar), but also for 5 bar ambient pressure conditions. Tables A1–A3 indicate the utilised fluid properties for 1 bar ambient pressure. The corresponding properties and the initial conditions for the base simulation cases in the case of 5 bar ambient pressure are summarised in Appendix A, Tables A4–A6, accordingly. Details regarding the varying parameters and the overall runs conducted for Series D of the parametric numerical simulations are summarised in Table 7.

As can be seen, a total of 30 simulations were performed. Four additional simulations for each of the considered working fluids (R113, R22 and R134a) were performed initially, changing the value of the gravitational acceleration from 9.81 m/s^2 in the base cases (D4, D9 and D14, Earth) to 0.58 m/s^2 (D1, D6 and D11, Pluto), 3.71 m/s^2 (D2, D7 and D12, Mars/Mercury), 8.83 m/s^2 (D3, D8 and D13, Venus/Saturn/Uranus) and 10.99 m/s^2 (D5, D10 and D15, Neptune). Then these simulations were all repeated (D16–D20 for R113, D20–D25 for R22 and D25–D30 for R134a), changing the ambient pressure from 1 to 5 bar, and hence the properties of the liquid and vapour phases (as summarised in

Tables A4–A6). The spatial evolution of the generated bubbles for each of the above cases, at the time of detachment, is depicted in Figures 24 and 25, for the 1 bar ambient pressure cases (D1–D15) and the 5 bar ambient pressure cases (D16–D30), respectively.

Table 7. Varied parameters in Series D of parametric numerical simulations.

Run	Gravitational Acceleration (m/s^2)	Working Fluid	Run	Gravitational Acceleration (m/s^2)	Working Fluid
D1	0.58 (Pluto)	R113	D16	0.58	R113
D2	3.71 (Mars/Mercury)	R113	D17	3.71	R113
D3	8.83 (Venus/Saturn/Uranus)	R113	D18	8.83	R113
D4 (base case, R113, P = 1 bar)	9.81 (Earth)	R113	D19 (base case, R113, P = 5 bar)	9.81	R113
D5	10.99 (Neptune)	R113	D20	10.99	R113
D6	0.58	R22	D21	0.58	R22
D7	3.71	R22	D22	3.71	R22
D8	8.83	R22	D23	8.83	R22
D9 (base case, R22, P = 1 bar)	9.81	R22	D24 (base case, R22, P = 5 bar)	9.81	R22
D10	10.99	R22	D25	10.99	R22
D11	0.58	R134a	D26	0.58	R134a
D12	3.71	R134a	D27	3.71	R134a
D13	8.83	R134a	D28	8.83	R134a
D14 (base case, R134a, P = 1 bar)	9.81	R134a	D29 (base case, R134a, P = 5 bar)	9.81	R134a
D15	10.99	R134a	D30	10.99	R134a

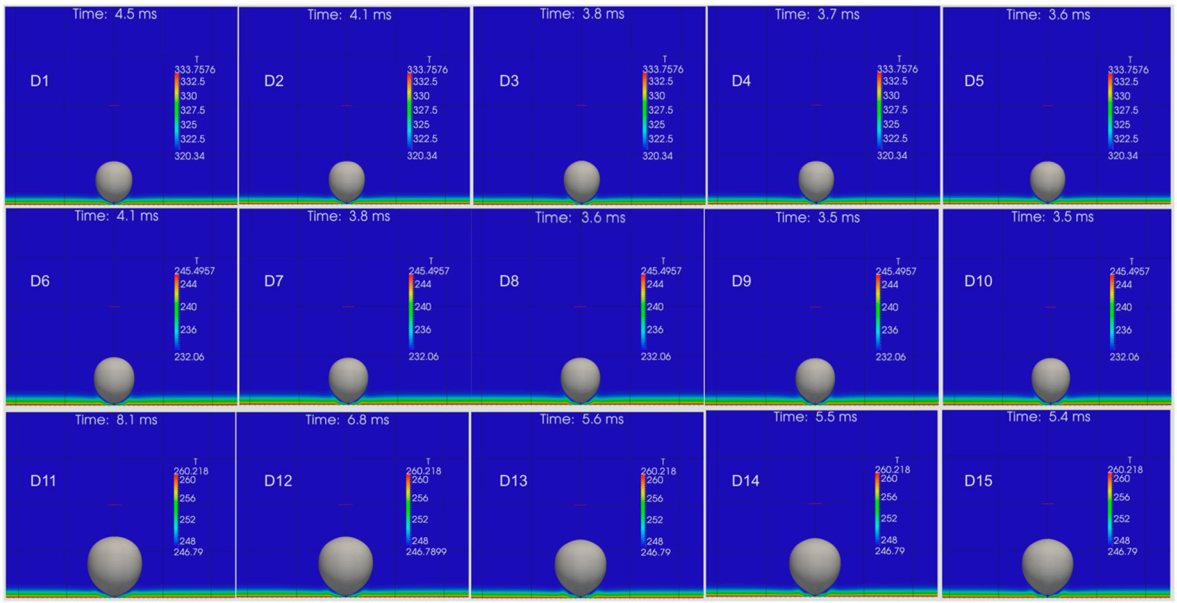

Figure 24. Spatial evolution of generated bubble at the time of detachment for each case of the Series D parametric numerical simulations, with the 1 bar ambient pressure condition.

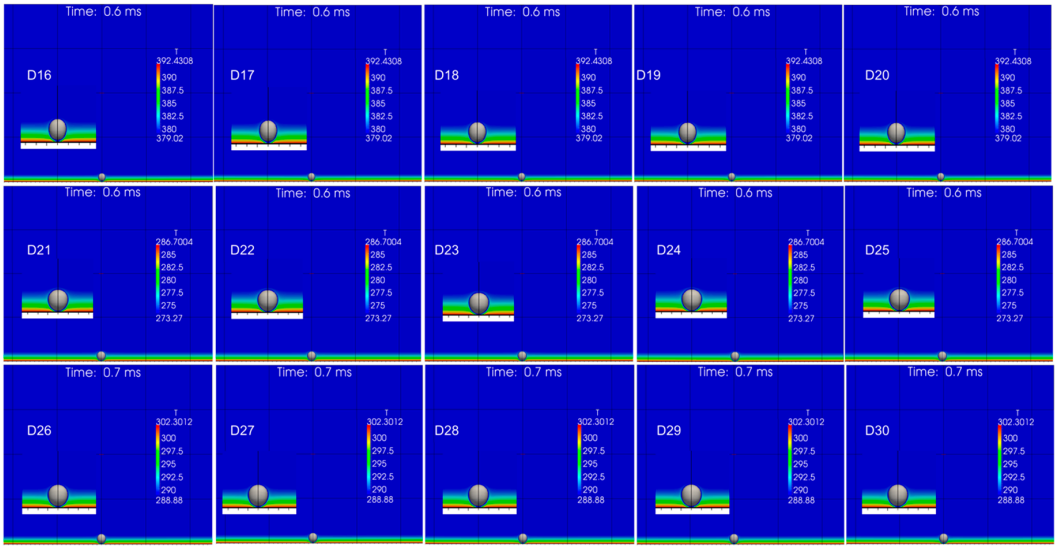

Figure 25. Spatial evolution of generated bubble at the time of detachment for each case of the Series D parametric numerical simulations, with the 5 bar ambient pressure condition.

As can be observed from Figure 24, for the cases of 1 bar ambient pressure, both the bubble detachment diameter as well as the bubble detachment time decreased with the corresponding increase of the gravity level. This observation can be explained by the corresponding increase of the acting buoyancy force on the generated bubble in each case bubble. In more detail, the higher the gravitational acceleration, the higher the acting buoyancy force, and therefore the lower the bubble detachment characteristics.

However, it is important to notice that for the cases of 5 bar ambient pressure (Figure 25), both the bubble detachment time as well as the bubble detachment volume seemed to be unaffected by the increase in the applied gravitational acceleration for all three of the examined working fluids. This can be seen in more detail in the diagrams of Figures 26 and 27, where the bubble detachment time (Figures 26a and 27a) as well as the equivalent bubble detachment diameter (Figures 26b and 27b) are plotted with respect to the applied gravitational acceleration for the cases of 1 bar (Figure 26) and 5 bar (Figure 27) ambient pressure, respectively.

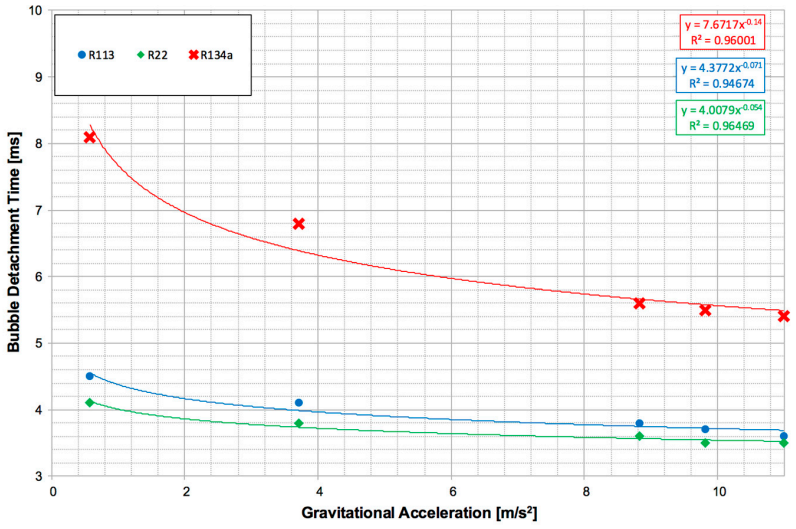

(**a**)

Figure 26. *Cont.*

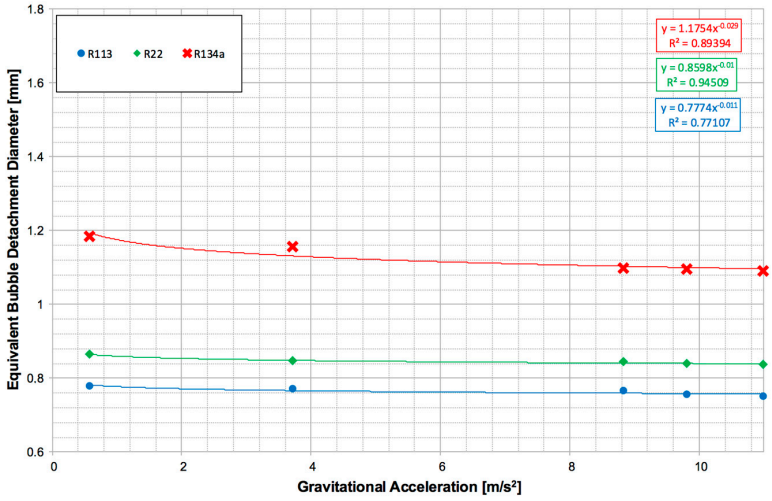

(**b**)

Figure 26. Effect of gravity level on: (**a**) the bubble detachment time; (**b**) the equivalent bubble detachment diameter (cases D1–D15, with the 1 bar ambient pressure condition).

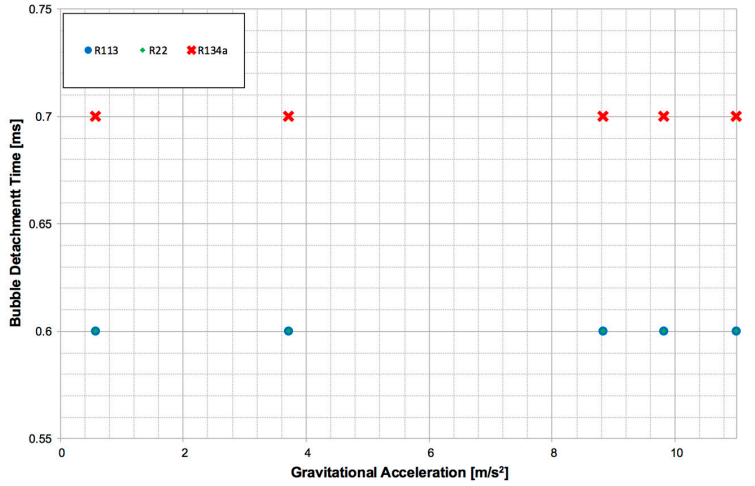

(**a**)

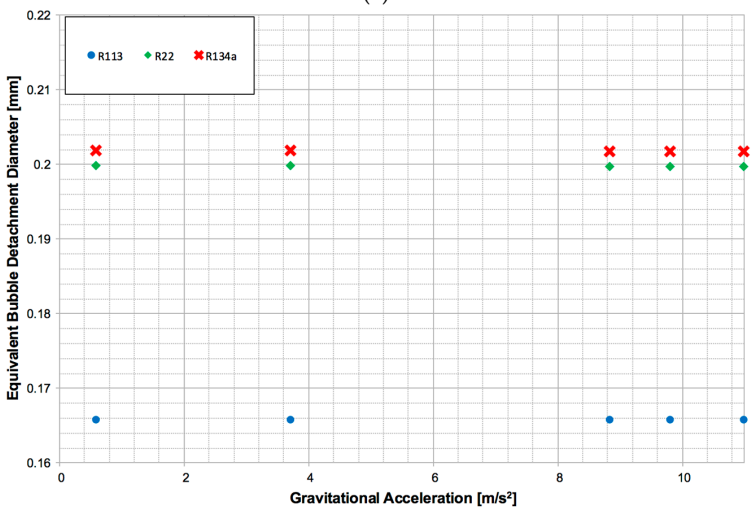

(**b**)

Figure 27. Effect of gravity level on: (**a**) the bubble detachment time; (**b**) the equivalent bubble detachment diameter (cases D16–D30, with the 5 bar ambient pressure condition).

As can be observed from Figure 26a, for all three of the examined working fluids, the bubble detachment time decreased with the corresponding increase in the applied gravitational acceleration, following a power law. It is characteristic to notice that the rate of decrease was initially higher for the case of R134a, while the other two considered refrigerants (R113 and R22) showed a similar rate of decrease in the bubble detachment time with respect to the corresponding increase in the gravity level. A similar overall behaviour could be observed for the equivalent bubble detachment diameter (Figure 26b). It is characteristic that a total variation of the gravitational acceleration by a factor of almost 19 caused a relatively low variation in the bubble detachment time and the equivalent bubble detachment diameters by a factor of 1.27 and 1.02, respectively.

Examining the diagrams of Figure 27, it can be concluded that, increasing the ambient pressure level of the system from 1 bar to 5 bar, it seems that the previously identified effects of the gravity level (Figure 26) are diminishing. Furthermore, it is evident that, in general, increasing the pressure level causes the bubble detachment characteristics to decrease significantly.

Finally, in order to compare the relative importance of the overall examined controlling parameters in the bubble detachment characteristics, Table 8 summarises the variation factors in the bubble detachment time and the equivalent bubble detachment diameter with respect to the corresponding variation factors for each of the examined controlling parameters, for the cases of the R113 refrigerant that are common to all of the conducted series of parametric numerical experiments.

Table 8. Comparison of relative importance of the effect of the examined controlling parameters in the bubble detachment characteristics (R113). Resulting change factors in the bubble detachment characteristics with respect to the maximum variation factors in the examined controlling parameters.

Controlling Parameter Variation Factor	t_{det} Variation Factor	D_{eq} Variation Factor
Initial Thermal Boundary Layer variation factor: 5	9	6
Contact Angle variation factor: 8	10	3
Heated Plate Superheat variation factor: 3.5	18	10
Gravitational acceleration variation factor: 18.9	1.27	1.02

As can be observed, according to the overall parametric numerical simulations, the heated plate superheat seems to be the most influential parameter on the bubble detachment characteristics. The influence of the ITBL and the surface wettability is also quite important. Finally, the gravitational acceleration seems to have a minor influence both on the bubble detachment time (t_{det}) and the equivalent bubble detachment diameter (D_{eq}).

5. Conclusions

From the overall analysis and discussion of the results, the following important conclusions can be drawn:

- Among the examined fundamental controlling parameters, it is shown that the heated plate superheat constitutes the most influential parameter, followed by the ITBL and the heated surface wettability (contact angle). For the examined flow conditions, the least influential parameter seems to be the applied gravitational acceleration.
- The bulk liquid thermal boundary layer thickness is a very influential parameter that should always be measured and reported in future experimental studies, since it comprises a required input for the successful numerical simulation of nucleate boiling processes.
- The bubble detachment characteristics seem to be significantly affected by the imposed contact angle (wettability of the heated plate) for values higher than the critical contact angle, which is equal to 45°. However, the proposed effect is minimal for contact angles lower than this limiting value of 45°. This finding leads for the first time to the identification of two distinct regions a "lyophilic" region for contact angles lower than 45° and a "lyophobic" region for contact angles higher than 45°.

- It is also found that the increase of the applied wall superheat causes a power law increase in both the bubble detachment time as well as the equivalent bubble detachment diameter, for all three of the examined working fluids. Temperature variations of even a few degrees can significantly alter the bubble detachment characteristics. Therefore, it can be concluded that the accurate measurement of the temperature value in the vicinity of the generated bubbles is quite crucial for the numerical reproduction of experimental results on nucleate boiling.
- For all three of the examined working fluids, both the bubble detachment time as well as the equivalent bubble detachment diameter decrease with the corresponding increase of the applied gravitational acceleration, following a power law. It is quite important that this power law effect on the bubble detachment characteristics almost disappears at pressure conditions higher than atmospheric pressure. This constitutes a quite useful finding for the design of experimental set-ups for micro-gravity and hyper-gravity experiments, and therefore it is worth further investigating the bubble detachment characteristics for a variety of different pressure levels below and above atmospheric pressure for the same gravitational acceleration values as the ones considered here.

In summary, the present investigation adds significantly to the existing knowledge on bubble growth and detachment in cases of saturated pool boiling of refrigerants, since a comprehensive examination of the effect of fundamental controlling parameters on isolated bubble detachment characteristics was conducted (more than 100 high-resolution, transient, numerical simulations were conducted for the purposes of the present investigation), identifying their exact quantitative influence on the bubble detachment diameter and time as well as their relative importance. Finally, it can be said that the use of the improved VOF-based interface-capturing approach, which was proposed, presented, validated and applied in the present investigation, constitutes a quite promising and novel tool for the simulation of bubble growth and detachment processes, providing great insight regarding the complex underlying physics, hydrodynamics and thermodynamics of such two-phase flow phenomena of significant interest for real technological applications.

In future investigations, the main aim is to develop a global simulation approach that is independent of empirical inputs such as the evaporation/condensation coefficient γ. Therefore, it is deemed appropriate to either substitute the model of Hardt and Wondra [19] with a more appropriate boiling model that does not depend on γ, or to couple the present VOF-based framework with an appropriate sub-model that provides the value of γ according to the global operating conditions.

Acknowledgments: Part of the results presented in the present paper constitute part of a wider research work, which was related to the development of a VOF-based flow boiling model, able to predict the bubble detachment characteristics in cases of diesel fuel flow boiling within injector nozzles, and it has received funding from the People Programme (IAPP Marie Curie Actions) of the European Union's Seventh Framework Programme FP7/2007-2013/under REA grant agreement No. 324313. The authors would also like to acknowledge the contribution of the super-computing facilities of CINECA, in Bologna (Italy), for the conduction of the large number of numerical simulations of the present investigation in a relatively short time. Part of the present work has also been carried forward in the framework of the ESA MAP Project INWIP. Therefore, the authors would also like to thank Olivier Minster and Balazs Toth for their interest and support.

Author Contributions: Anastasios Georgoulas and Marco Marengo developed, validated and partially applied the code for one of the working fluids considered. Manolia Andredaki performed all the additional parametric simulations and the overall post-processing of the numerical runs. All authors contributed equally in the analysis of the overall data, the writing and revision of the present paper.

Conflicts of Interest: The authors declare no conflict of interest.

Appendix A

Table A1. Fluid properties and initial conditions (base case for R113, Series A–D).

		ρ (kg/m^3)	c_p (J/kgK)	k (W/mK)	ν (m^2/s)	σ (N/m)	h_{lv}(J/kg)
Phase properties (R113 at 1 bar, T_{sat} = 320.65 K)	Liquid	1508.4	940.3	0.064	3.25×10^{-7}	0.015	144,350
	Vapour	7.4	691.3	0.0095	1.39×10^{-6}		
Initial Conditions	Initial bubble (seed) radius (μm): 50		Wall superheat (K): 13.5			Domain size (mm): 2.5 × 4.0	
			Contact angle (°): 11.4 (Series A), 30 (Series B–D)				
	Initially developed thermal boundary layer thickness (μm): 352		Simulation Type: Axisymmetric			No. of computational cells: 400,000	

Table A2. Fluid properties and initial conditions (base case for R22, Series B–D).

		ρ (kg/m^3)	c_p (J/kgK)	k (W/mK)	ν (m^2/s)	σ (N/m)	h_{lv}(J/kg)
Phase properties (R22 at 1 bar, T_{sat} = 232.06 K	Liquid	1410.0	1089.2	0.1135	2.46×10^{-7}	0.015	217,160
	Vapour	4.65	605.61	0.0070	1.88×10^{-6}		
Initial Conditions	Initial bubble (seed) radius (μm): 50		Wall superheat (K): 13.5			Domain size (mm): 2.5 × 4.0	
			Contact angle (°): 30				
	Initially developed thermal boundary layer thickness (μm): 352		Simulation Type: Axisymmetric			No. of computational cells: 400,000	

Table A3. Fluid properties and initial conditions (base case for R134a, Series B–D).

		ρ (kg/m^3)	c_p (J/kgK)	k (W/mK)	ν (m^2/s)	σ (N/m)	h_{lv}(J/kg)
Phase properties (R134a at 1 bar, T_{sat} = 246.79 K)	Liquid	1377.5	1280.0	0.104	2.76×10^{-7}	0.015	144,350
	Vapour	5.19	793.19	0.0093	1.39×10^{-6}		
Initial Conditions	Initial bubble (seed) radius (μm): 50		Wall superheat (K): 13.5			Domain size (mm): 2.5 × 4.0	
			Contact angle (°): 30				
	Initially developed thermal boundary layer thickness (μm): 352		Simulation Type: Axisymmetric			No. of computational cells: 400,000	

Table A4. Fluid properties and initial conditions (base case for R113, at 5 bar).

		ρ (kg/m^3)	c_p (J/kgK)	k (W/mK)	ν (m^2/s)	σ (N/m)	h_{lv}(J/kg)
Phase properties (R113 at 5 bar, T_{sat} = 379.02 K)	Liquid	1351.4	1014.9	0.053	1.94×10^{-3}	0.0086	122,950
	Vapour	34.1	790.8	0.012	3.56×10^{-3}		
Initial Conditions	Initial bubble (seed) radius (μm): 50		Wall superheat (K): 13.5			Domain size (mm): 2.5 × 4.0	
			Contact angle (°): 30				
	Initially developed thermal boundary layer thickness (μm): 352		Simulation Type: Axisymmetric			No. of computational cells: 400,000	

Table A5. Fluid properties and initial conditions (base case for R22, at 5 bar).

		ρ (kg/m^3)	c_p (J/kgK)	k (W/mK)	ν (m^2/s)	σ (N/m)	h_{lv}(J/kg)
Phase properties (R22 at 5 bar) T_{sat} = 273.27 K	Liquid	1281.1	1169.6	0.094687	1.68×10^{-3}	0.01168	144,350
	Vapour	21.312	739.50	0.009416	5.33×10^{-3}		
Initial Conditions	Initial bubble (seed) radius (μm): 50		Wall superheat (K): 13.5			Domain size (mm): 2.5 × 4.0	
			Contact angle (°): 30				
	Initially developed thermal boundary layer thickness (μm): 352		Simulation Type: Axisymmetric			No. of computational cells: 400,000	

Table A6. Fluid properties and initial conditions (base case for R134a, at 5 bar).

		ρ (kg/m^3)	c_p (J/kgK)	k (W/mK)	ν (m^2/s)	σ (N/m)	h_{lv}(J/kg)
Phase properties (R134a at 1 bar) T_{sat} = 246.79 K	Liquid	1240.8	1389.4	0.085126	1.76×10^{-3}	0.00934	185,970
	Vapour	24.317	976.12	0.012930	4.70×10^{-3}		
Initial Conditions	Initial bubble (seed) radius (μm): 50		Wall superheat (K): 13.5			Domain size (mm): 2.5 × 4.0	
			Contact angle (°): 30				
	Initially developed thermal boundary layer thickness (μm): 352		Simulation Type: Axisymmetric			No. of computational cells: 400,000	

References

1. Nelson, R.A. Do we doubt too little? Examples from the thermal sciences. *Exp. Therm. Fluid Sci.* **2001**, *25*, 255–267. [CrossRef]
2. Wagner, E.; Sodtke, C.; Schweizer, N.; Stephan, P. Experimental study of nucleate boiling heat transfer under low gravity conditions using TLCs for high resolution temperature measurements. *Heat Mass Transf.* **2006**, *42*, 875–883. [CrossRef]
3. Baldassari, C.; Mameli, M.; Marengo, M. Non-Uniform Onset of Nucleate Flow Boiling of R-134a Inside a Glass Minichannel. *Exp. Heat Transf.* **2014**, *27*, 316–328. [CrossRef]
4. Hassan, Y.A.; Estrada-Perez, C.E.; Yoo, J.S. Measurement of subcooled flow boiling using Particle Tracking Velocimetry and infrared thermographic technique. *Nucl. Eng. Des.* **2014**, *268*, 185–190. [CrossRef]
5. Delgoshaei, P.; Kim, J. Microscale Heat Transfer Measurements During Subcooled Pool Boiling of Pentane: Effect of Bubble Dynamics. In Proceedings of the 14th International Heat Transfer Conference, Washington, DC, USA, 8–13 August 2010; ASME Digital Collection: Wshington, DC, USA, 2010; pp. 397–405.
6. Wagner, E.; Stephan, P.; Koeppen, O.; Auracher, H. High resolution temperature measurements at moving vapor/liquid and vapor/liquid/solid interfaces during bubble growth in nucleate boiling. *Fortschr. Ber. VDI* **2007**, *3*, 260–277.
7. Sempértegui, D.; Ribatski, G. Micro-Scale Flow Pattern Classification Based on the K-Means Clustering Algorithm. In Proceedings of the ASME 2010 8th International Conference on Nanochannels, Microchannels, and Minichannels Collocated with 3rd Joint US-European Fluids Engineering Summer Meeting, Montreal, QC, Canada, 1–5 August 2010; pp. 1619–1627.
8. Kurul, N.; Podowski, M.Z. Multidimensional effects in forced convection subcooled boiling. In Proceedings of the 9th International Heat Transfer Conference, Jerusalem, Israel, 19–24 August 1990; pp. 19–24.
9. Prabhudharwadkar, D.; Lopez-de-Bertodano, M.A.; Hibiki, T.; Buchanan, J.R. Assessment of subcooled boiling wall boundary correlations for two-fluid model CFD. *Int. J. Heat Mass Transf.* **2014**, *79*, 602–617. [CrossRef]
10. Cheung, S.C.P.; Vahaji, S.; Yeoh, G.H.; Tu, J.Y. Modeling subcooled flow boiling in vertical channels at low pressures—Part 1: Assessment of empirical correlations. *Int. J. Heat Mass Transf.* **2014**, *75*, 736–753. [CrossRef]
11. Unverdi, S.O.; Tryggvason, G. A front-tracking method for viscous, incompressible, multi-fluid flows. *J. Comput. Phys.* **1992**, *100*, 25–37. [CrossRef]

12. Tryggvason, G.; Bunner, B.; Esmaeeli, A.; Juric, D.; Al-Rawahi, N.; Tauber, W.; Han, J.; Nas, S.; Jan, Y.-J. A Front-tracking Method for the Computations of Multiphase Flow. *J. Comput. Phys.* **2001**, *169*, 708–759. [CrossRef]
13. Esmaeeli, A.; Tryggvason, G. Computations of film boiling. Part I: Numerical method. *Int. J. Heat Mass Transf.* **2004**, *47*, 5451–5461. [CrossRef]
14. Esmaeeli, A.; Tryggvason, G. Computations of film boiling. Part II: Multi-mode film boiling. *Int. J. Heat Mass Transf.* **2004**, *47*, 5463–5476. [CrossRef]
15. Fuchs, T.; Kern, J.; Stephan, P. A Transient Nucleate Boiling Model Including Microscale Effects and Wall Heat Transfer. *J. Heat Transf.* **2006**, *128*, 1257–1265. [CrossRef]
16. Welch, S.W.J.; Rachidi, T. Numerical Computation of Film Boiling Including Conjugate Heat Transfer. *Numer. Heat Transf. Part B Fundam.* **2002**, *42*, 35–53. [CrossRef]
17. Welch, S.W.J.; Wilson, J. A Volume of Fluid Based Method for Fluid Flows with Phase Change. *J. Comput. Phys.* **2000**, *160*, 662–682. [CrossRef]
18. Aus der Wiesche, S. Bubble growth and departure during nucleate boiling: The occurrence of heat flux reversal. In Proceedings of the 4th International Conference on Computational Heat and Mass Transfer, Paris, France, 17–20 May 2005.
19. Hardt, S.; Wondra, F. Evaporation model for interfacial flows based on a continuum-field representation of the source terms. *J. Comput. Phys.* **2008**, *227*, 5871–5895. [CrossRef]
20. Ose, Y.; Kunugi, T. Numerical Study on Sabcooled Pool Boiling. *Prog. Nucl. Sci. Technol.* **2011**, *2*, 125–129. [CrossRef]
21. Ose, Y.; Kunugi, T. Development of A Boiling and Condensation Model on Subcooled Boiling Phenomena. *Energy Procedia* **2011**, *9*, 605–618. [CrossRef]
22. Kunkelmann, C.; Ibrahem, K.; Schweizer, N.; Herbert, S.; Stephan, P.; Gambaryan-Roisman, T. The effect of three-phase contact line speed on local evaporative heat transfer: Experimental and numerical investigations. *Int. J. Heat Mass Transf.* **2012**, *55*, 1896–1904. [CrossRef]
23. Kunkelmann, C.; Stephan, P. CFD Simulation of Boiling Flows Using the Volume-of-Fluid Method within OpenFOAM. *Numer. Heat Transf. Part A Appl.* **2009**, *56*, 631–646. [CrossRef]
24. Kunkelmann, C. Numerical Modeling and Investigation of Boiling Phenomena. Ph.D. Thesis, Technische Universität Darmstadt, Darmstadt, Germany, 2011.
25. Sato, Y.; Ničeno, B. A sharp-interface phase change model for a mass-conservative interface tracking method. *J. Comput. Phys.* **2013**, *249*, 127–161. [CrossRef]
26. Son, G.; Dhir, V.K.; Ramanujapu, N. Dynamics and Heat Transfer Associated With a Single Bubble during Nucleate Boiling on a Horizontal Surface. *J. Heat Transf.* **1999**, *121*, 623–631. [CrossRef]
27. Dhir, V.K. Numerical simulations of pool-boiling heat transfer. *AIChE J.* **2001**, *47*, 813–834. [CrossRef]
28. Lee, W.; Son, G.; Yoon, H.Y. Numerical study of bubble growth and boiling heat transfer on a microfinned surface. *Int. Commun. Heat Mass Transf.* **2012**, *39*, 52–57. [CrossRef]
29. Gibou, F.; Chen, L.; Nguyen, D.; Banerjee, S. A Level Set Based Sharp Interface Method for the Multiphase Incompressible Navier-Stokes Equations with Phase Change. *J. Comput. Phys.* **2007**, *222*, 536–555. [CrossRef]
30. Rueda Villegas, L.; Alis, R.; Lepilliez, M.; Tanguy, S. A Ghost Fluid/Level Set Method for boiling flows and liquid evaporation: Application to the Leidenfrost effect. *J. Comput. Phys.* **2016**, *316*, 789–813. [CrossRef]
31. Tanguy, S.; Sagan, M.; Lalanne, B.; Couderc, F.; Colin, C. Benchmarks and numerical methods for the simulation of boiling flows. *J. Comput. Phys.* **2014**, *264*, 1–22. [CrossRef]
32. Shu, B.; Ingenieure, V.D. *Numerische Simulation des Blasensiedens Mit Volume-of-Fluid- und Level-Set-Methode*; VDI Verlag: Düsseldorf, Germany, 2010.
33. Kunkelmann, C.; Stephan, P. Numerical simulation of the transient heat transfer during nucleate boiling of refrigerant HFE-7100. *Int. J. Refrig.* **2010**, *33*, 1221–1228. [CrossRef]
34. Hazi, G.; Markus, A. On the bubble departure diameter and release frequency based on numerical simulation results. *Int. J. Heat Mass Transf.* **2009**, *52*, 1472–1480. [CrossRef]
35. Badillo, A. Quantitative phase-field modeling for boiling phenomena. *Phys. Rev. E* **2012**, *86*, 41603. [CrossRef] [PubMed]
36. Georgoulas, A.; Koukouvinis, P.; Gavaises, M.; Marengo, M. Numerical investigation of quasi-static bubble growth and detachment from submerged orifices in isothermal liquid pools: The effect of varying fluid properties and gravity levels. *Int. J. Multiph. Flow* **2015**, *74*, 59–78. [CrossRef]

37. Magnini, M.; Pulvirenti, B. Height function interface reconstruction algorithm for the simulation of boiling flows. In *WIT Transactions on Engineering Sciences*; WIT Press: Southampton, UK, 2011; Volume 70, pp. 69–80.
38. Lee, H.C.; Do Oh, B.; Bae, S.W.; Kim, M.H. Single bubble growth in saturated pool boiling on a constant wall temperature surface. *Int. J. Multiph. Flow* **2003**, *29*, 1857–1874. [CrossRef]
39. Brackbill, J.; Kothe, D.; Zemach, C. A continuum method for modeling surface tension. *J. Comput. Phys.* **1992**, *100*, 335–354. [CrossRef]
40. Hoang, D.A.; van Steijn, V.; Portela, L.M.; Kreutzer, M.T.; Kleijn, C.R. Benchmark numerical simulations of segmented two-phase flows in microchannels using the Volume of Fluid method. *Comput. Fluids* **2013**, *86*, 28–36. [CrossRef]
41. Deshpande, S.S.; Anumolu, L.; Trujillo, M.F. Evaluating the performance of the two-phase flow solver interFoam. *Comput. Sci. Discov.* **2012**, *5*, 14016. [CrossRef]
42. OpenFOAM. The Open Source CFD Toolbox, User Guide. 2013. Available online: https://cfd.direct/openfoam/user-guide/ (accessed on 24 Febuary 2017).
43. Scardovelli, R.; Zaleski, S. Direct Numerical Simulation of Free-Surface and Interfacial Flow. *Annu. Rev. Fluid Mech.* **1999**, *31*, 567–603. [CrossRef]
44. Schrage, R.W. *A Theoretical Study of Interphase Mass Transfer*; Columbia University Press: New York, NY, USA, 1953.
45. Kunkelmann, C.; Stephan, P. Modification and extension of a standard volume-of-fluid solver for simulating boiling heat transfer. In Proceedings of the 5th European Conference on Computational Fluid Dynamics, Lisbon, Portugal, 14–17 June 2010.
46. Magnini, M. *CFD Modeling of Two-Phase Boiling Flows in the Slug Flow Regime with an Interface Capturing Technique*; University of Bologna: Bologna, Italy, 2012.
47. Plesset, M.S.; Zwick, S.A. The Growth of Vapor Bubbles in Superheated Liquids. *J. Appl. Phys.* **1954**, *25*, 493–500. [CrossRef]
48. Scriven, L.E. On the dynamics of phase growth: L.E. Scriven, Chem. Engng. Sci.10: 1–13, 1959. *Chem. Eng. Sci.* **1995**, *50*, 3905. [CrossRef]
49. Mukherjee, A.; Kandlikar, S.G. Numerical study of single bubbles with dynamic contact angle during nucleate pool boiling. *Int. J. Heat Mass Transf.* **2007**, *50*, 127–138. [CrossRef]
50. Gong, S.; Cheng, P. Numerical simulation of pool boiling heat transfer on smooth surfaces with mixed wettability by lattice Boltzmann method. *Int. J. Heat Mass Transf.* **2015**, *80*, 206–216. [CrossRef]
51. Liao, J.; Mei, R.; Klausner, J.F. The influence of the bulk liquid thermal boundary layer on saturated nucleate boiling. *Int. J. Heat Fluid Flow* **2004**, *25*, 196–208. [CrossRef]
52. Dhir, V.K. Mechanistic Prediction of Nucleate Boiling Heat Transfer–Achievable or a Hopeless Task? *J. Heat Transf.* **2005**, *128*, 1–12. [CrossRef]
53. Bourdon, B.; Rioboo, R.; Marengo, M.; Gosselin, E.; De Coninck, J. Influence of the Wettability on the Boiling Onset. *Langmuir* **2012**, *28*, 1618–1624. [CrossRef] [PubMed]
54. Bourdon, B.; Bertrand, E.; Di Marco, P.; Marengo, M.; Rioboo, R.; De Coninck, J. Wettability influence on the onset temperature of pool boiling: Experimental evidence onto ultra-smooth surfaces. *Adv. Colloid Interface Sci.* **2015**, *221*, 34–40. [CrossRef] [PubMed]
55. Nam, Y.; Wu, J.; Warrier, G.; Ju, Y.S. Experimental and Numerical Study of Single Bubble Dynamics on a Hydrophobic Surface. *J. Heat Transf.* **2009**, *131*, 121004. [CrossRef]
56. Malavasi, I.; Bourdon, B.; Di Marco, P.; de Coninck, J.; Marengo, M. Appearance of a low superheat "quasi-Leidenfrost" regime for boiling on superhydrophobic surfaces. *Int. Commun. Heat Mass Transf.* **2015**, *63*, 1–7. [CrossRef]
57. Sanna, A. Numerical Investigation of Saturated Flow Boiling on Thin Walls. Ph.D. Thesis, Brunel University, London, UK, 2010.